High-resolution velocity measurement in the inner part of turbulent boundary layers over super-hydrophobic surfaces

Citation	Ling, Hangjian et al. "High-Resolution Velocity Measurement in the Inner Part of Turbulent Boundary Layers over Super-Hydrophobic Surfaces." Journal of Fluid Mechanics 801 (July 2016): 670–703 © 2016 Cambridge University Press
As Published	http://dx.doi.org/10.1017/JFM.2016.450
Publisher	Cambridge University Press (CUP)
Version	Author's final manuscript
Citable link	http://hdl.handle.net/1721.1/120091
Terms of Use	Creative Commons Attribution-Noncommercial-Share Alike
Detailed Terms	http://creativecommons.org/licenses/by-nc-sa/4.0/

High resolution velocity measurement in the inner part of turbulent boundary layers over super-hydrophobic surfaces

H. Ling[1], S. Srinivasan[2], K. Golovin[3], G. Mckinley[2], A. Tuteja[3] and J. Katz[1]†

[1]Department of Mechanical Engineering, Johns Hopkins University, Baltimore, MD 21218, USA
[2]Department of Mechanical Engineering, Massachusetts Institute of Technology, Cambridge, MA 02139, USA
[3]Department of Materials Science and Engineering, University of Michigan, Ann Arbor, MI 48109, USA

†Email address for correspondence: katz@jhu.edu

(Received ?; revised ?; accepted ?. –To be entered by editorial office)

Digital holographic microscopy is used for characterizing the profiles of mean velocity, viscous and Reynolds shear stresses, as well as turbulence level in the inner part of turbulent boundary layers over several super-hydrophobic surfaces (SHSs) with varying roughness/texture characteristics. The friction Reynolds numbers vary from 693 to 4496, and the normalized rms values of roughness (k_{rms}^+) vary from 0.43 to 3.28. The wall shear stress is estimated from the sum of the viscous and Reynolds shear stress at the top of roughness elements, and the slip velocity is obtained from the mean profile at the same elevation. For flow over SHSs with $k_{rms}^+<1$, drag reduction and an upward shift of the mean velocity profiles occur, along with a mild increase in turbulence in the inner part of the boundary layer. As the roughness increases above $k_{rms}^+\sim1$, the flow over the SHSs transitions from drag reduction, where the viscous stress dominates, to drag increase where the Reynolds shear stress becomes the primary contributor. For the present maximum value of $k_{rms}^+=3.28$, the inner region exhibits the characteristics of a rough wall boundary layer, including elevated wall friction and turbulence, as well as a downward shift in the mean velocity. Increasing the pressure in the test facility to a level that compresses the air layer in the SHSs and exposes the protruding roughness elements reduces the extent of drag reduction. Alignment of the roughness elements in the streamwise direction increases the drag reduction. For SHSs where the roughness effect is not dominant ($k_{rms}^+<1$), the present measurements confirm previous theoretical predictions of the relationships between drag reduction and slip velocity allowing for both spanwise and streamwise slip contributions.

Key words: xxx; xxx;

1. Introduction

Over the last decade, there has been a growing interest in fluid motion close to super-hydrophobic surfaces (SHSs) due to their potential application for drag reduction, initially in laminar flows (Rothstein 2010, Watanabe *et al.* 1999), and recently in turbulent boundary layers as well (Bidkar *et al.* 2014, Min & Kim 2004, Park *et al.* 2014). SHSs are typically constructed using a combination of micro- or/and nano-scale texture features and a hydrophobic surface chemistry (Liu *et al.* 2013). The hydrophobicity increases the local contact angle at the three phase contact line. Hence, it promotes the retention of micro air pockets between the asperities of the roughness, creating a partial air layer that separates the solid wall from the liquid (Rothstein 2010). The net effect is similar to that achieved by injecting microbubbles in attempts to create lubricating air layers (Ceccio 2010), but typically requires no energy input. However, when the textured surface is fully wetted and the dimensionless roughness expressed in wall units, $k^+=k/\delta_\upsilon$, exceeds a critical value (Jimenez 2004), the roughness increases the wall friction in turbulent boundary layers. Here, k is the roughness height and δ_υ is viscous length scale (υ/u_τ, the ratio between kinematic viscosity and friction velocity). The published values of k^+ for the onset of transition from smooth to rough regimes varies from $k^+=0.1$ (Unal *et al.* 2012),

$k^+=1$ (Schultz & Flack 2007, Shockling *et al.* 2006) to 15 (Ligrani & Moffat 1986), depending on the roughness type and uniformity. Therefore, SHSs consisting of rough boundaries may cause either drag increase, or reduction, depending on the roughness characteristics and Reynolds number *Re* of the flow. Bidkar *et al.* (2014) have recently reported that k^+ needs to be smaller than 0.5 for successful drag reduction, at least for the geometry used in their study. The objective of the present paper is to elucidate the competition and interplay between hydrophobicity and roughness effects through high-resolution near wall velocity measurements within turbulent boundary layers developing over SHSs.

Numerical simulations have predicted appreciable turbulent drag reduction by SHSs, and have provided valuable physical insight into the processes involved. Most of these simulations have assumed ideal conditions, e.g., a flat air-water interface and no air loss. Simple surface textures have been simulated, such as posts (Martell *et al.* 2010), ridges (Jelly *et al.* 2014), and sinusoidal grooves (Hasegawa *et al.* 2011). The solid-liquid and air-liquid interfaces have been modeled either separately as no-slip and shear-free boundaries (Martell *et al.* 2009), or combined as an effective slip boundary (Min & Kim 2004, You & Moin 2007), i.e., by assuming that:

$$u\big|_{y=0}=u_s=\lambda_x\left.\frac{\partial u}{\partial y}\right|_{y=0},\qquad v\big|_{y=0}=0,\qquad w\big|_{y=0}=w_s=\lambda_z\left.\frac{\partial w}{\partial y}\right|_{y=0} \tag{1}$$

where u, v, and w are the streamwise (x), wall-normal (y), and spanwise (z) velocity components, respectively, u_s and w_s are the slip velocity components at the wall, and λ_x and λ_z are components of the so-called slip lengths in directions indicated by the subscript. The existence of a non-zero streamwise slip length has several effects: (i) Significant drag reduction occurs when λ_x is on the order of δ_υ or larger, and this effect increases with $\lambda_x^+=\lambda_x/\delta_\upsilon$ (Park *et al.* 2013a). For example, using direct numerical simulation (DNS), reduction of drag by more than 50% has been predicted by Martell *et al.* (2010), Busse & Sandham (2012), and Park *et al.* (2013a). (ii) The mean velocity profile is shifted upward by u_s^+ (Jeffs *et al.* 2010) compared to that of the smooth wall. (iii) The peak magnitudes of all Reynolds stress components are significantly reduced but there is non-zero turbulence at the interface (Jelly *et al.* 2014). (iv) The streamwise vortical structures are suppressed (Park *et al.* 2013a) and near wall streaks are weakened (Busse & Sandham 2012, Min & Kim 2004). However, the existence of a finite spanwise slip length has opposite effects, such as an increase in drag and Reynolds stresses, as well as a downward shift in the mean velocity profile (Fukagata *et al.* 2006). When both λ_x and λ_z are non-zero, drag reduction is expected to be achieved when $\lambda_x \geq \lambda_z$ or when $\lambda_x^+>3.5$ for all values of λ_z (Busse & Sandham 2012). High values of λ_x and λ_z can be obtained by increasing the air fraction of the SHSs, e.g., by increasing the spacing between micro-features for a fixed feature size (Jeffs *et al.* 2010).

In reality, the air-water interface is neither flat nor steady, and the air layer can be continuously entrained by the liquid (Samaha *et al.* 2011, 2012, Seo *et al.* 2015), leading to a wetting transition and exposing the rough surface texture. Hence, it is essential to perform detailed velocity measurements near the SHS surface at realistic Reynolds numbers, which can be used for determining both the slip velocity and the local shear stresses. Furthermore, for large scale applications, SHSs with random roughness are simpler to manufacture and apply than the idealized geometrical textures used in simulations, e.g., by spraying (Srinivasan *et al.* 2011) or sand-blasting (Peguero & Breuer 2009). One would expect that the behavior of a boundary layer over a random roughness pattern is different from that of e.g., structured posts or ridges, considering that streamwise aligned ridges can reduce drag by themselves (Choi *et al.* 1993, Garcia-Mayoral & Jimenez 2011) regardless of surface chemistry. Yet, as will be shown in this study, the key findings of these earlier numerical and theoretical studies are broadly consistent with the experimental trends for random SHSs as well.

In parallel, numerous experimental studies have investigated the performance of SHSs in turbulent boundary layers (Charles *et al.* 2006), channel flow (Daniello *et al.* 2009), and Taylor-Couette flow (Greidanus *et al.* 2011, Srinivasan *et al.* 2015). These tests have evaluated regularly patterned SHSs, such as ridges (Park *et al.* 2013b) and posts (Charles *et al.* 2006), as well as random roughness (Aljallis *et al.* 2013). The texture or roughness heights have ranged from nano-scale (Zhao *et al.* 2007) to tens of microns (Bidkar *et al.* 2014). The skin-frictions exerted on the textured surface have been quantified using floating surfaces connected to strain gages (Bidkar *et al.* 2014), as well as measuring the torque on the inner rotor in a Taylor-Couette facility (Greidanus *et al.* 2011, Srinivasan *et al.* 2015), or the pressure drop in a channel flow (Jung & Bhushan 2010). Studies involving application of Particle Image Velocimetry (PIV) have typically resolved only the buffer and outer parts of the boundary layer ($y>5\delta_\upsilon$) (Daniello *et al.* 2009, Peguero & Breuer 2009, Tian *et al.* 2015, Woolford *et al.* 2009). The velocity distributions have been used for examining the effect of SHSs on the flow structures and on the wall friction, the latter by fitting the mean velocity profiles in the log region (Tian *et al.* 2015), or by linearly extending the total stress profiles to the wall (Woolford *et al.* 2009). In a subset of these experiments, there has been no observable drag reduction, which the authors and later researchers have postulated to be a result of air layer depletion (Aljallis *et al.* 2013), air layer vibrations (Peguero & Breuer 2009, Zhao *et al.* 2007), dominance of wall roughness effects (Bidkar *et al.* 2014), as well as measurement uncertainties and errors (Greidanus *et al.* 2011). However, other studies have successfully detected drag reduction with values that are consistent with the numerical results. In particular, they show that: (i) The drag reduction increases with increasing gas fraction (Park *et al.* 2013b, 2014) and *Re*, at least for setups involving channels at moderate *Re* (Daniello *et al.* 2009) and Taylor-Couette flows over a broad range of conditions (Srinivasan *et al.* 2015). For example, a maximum of 75% reduction is reported by Park *et al.* (2013b, 2014) for SHSs consisting of streamwise-aligned micro-ridges with a 95% gas fraction. (ii) By using spanwise-aligned ridges, Woolford *et al.* (2009) argue that spanwise slip increases drag. (iii) The mean velocity profile is shifted upward and the peak Reynolds shear stress decreases for $\lambda_x>0$ (Tian *et al.* 2015, Woolford *et al.* 2009). Conversely, for $\lambda_z>0$, the mean velocity is shifted downward, and the Reynolds stress increases (Woolford *et al.* 2009).

Several notable theoretical studies have also attempted to predict and model the turbulent drag reduction induced by SHSs. Fukagata *et al.* (2006) have introduced a functional relationship between drag reduction and slip length by matching the bulk mean velocity of the no-slip flow to that of the slip flow in the log region

$$u_{\tau 0}\left(\frac{1}{\kappa}\log\left(\mathrm{Re}_\tau u_{\tau 0}/u_\tau\right)+F\left(\lambda_z^+=0\right)\right)=u_\tau\left(\lambda_x^+ +\frac{1}{\kappa}\log\left(\mathrm{Re}_\tau\right)+F\left(\lambda_z^+\right)\right) \tag{2}$$

Here $u_{\tau 0}$ is the friction velocity of the no-slip flow, κ=0.41 is the von Karman constant, $Re_\tau=u_\tau\delta/\upsilon$ is the friction Reynolds number (δ is the boundary layer thickness), and $F(\lambda_z^+)$ is a function of λ_z^+. For the no-slip flow, $F(\lambda_z^+=0)=3.2$ (Dean 1978). For the slip flow, $F(\lambda_z^+)$ is obtained from empirical fitting to DNS results for flow with only spanwise slip. This model assumes that the effects of spanwise slip and streamwise slip are independent of each other, that κ does not change, and that drag reduction is caused solely by modification to the mean velocity profile. Substituting the λ_x^+, λ_z^+ and Re_τ in Eqn. 2, the calculated ratio of $u_\tau/u_{\tau 0}$ agrees with their DNS results. Subsequently, Busse & Sandham (2012) have proposed a modified $F(\lambda_z^+)$, which requires less parameters for fitting the numerical simulation data. For SHSs in Taylor-Couette flows, Srinivasan et al. (2015) have proposed a modified Prandtl–von Kármán–type law to relate the skin friction coefficient to the slip length that is consistent within their range of Reynolds number (10 000<*Re*<80 000). For SHSs comprised of periodic post arrays, Seo & Mani (2015) have introduced a model for slip length as a function of the cubic root of the pattern wavelength, which agrees with their DNS results.

In summary, both numerical simulations, and a number of prior experiments, have shown great promise for applying SHSs for turbulent drag reduction. However, due to the limited resolution of previous experimental studies, direct measurements of several key features are still unavailable. For example, the impact of SHSs on the profiles of mean velocity and turbulent parameters in the inner parts of boundary layers ($y<5\delta_\upsilon$) remains unclear. Importantly, the relative contributions between viscous and Reynolds stress components has not been resolved considering that slip can occur over a substantial fraction of the wall. Furthermore, the slip velocity and the slip length have not been measured directly in turbulent flows. Thus, the functional relations between λ_x^+, λ_z^+ and drag reduction proposed in the theoretical (Busse & Sandham 2012, Fukagata *et al.* 2006) and numerical (Park *et al.* 2013a) studies have not been verified. Thus, the present paper focuses on measuring the flow structure and Reynolds stresses very close to the wall ($y<5\delta_\upsilon$) for several different SHSs, including direct measurements of the local wall friction and slip velocity. By extending the range of boundary layer Reynolds numbers, we also show that a single surface can transition from reducing drag to increasing the drag, as k^+ increases above a certain threshold level, corresponding to when the roughness effects dominate. To maintain and replenish the air layer, porous substrates for the SHSs are also used with controlled pressure across the porous wall. The experimental setup is described in Section 2, followed by presentation of results in Section 3, and a discussion and conclusions in Section 4.

2. Experimental Setup and Techniques

The experiments have been performed in a small, high-speed water tunnel described in Gopalan & Katz (2000) and Liu & Katz (2006). The flow is driven by two 15 HP (maximum) centrifugal pumps located 5 m below the test section, and passes through a settling tank, an electromagnetic flow meter, a settling chamber containing honeycombs and screen, as well as a 9:1 contraction before entering the test section. Components relevant to the present study, as they are installed in the 406 mm long, 61 mm high and 50 mm wide transparent test section, are sketched in figure 1(a). The mean tunnel speeds (flow rate divided by the tunnel cross section), U_m, are between 2 to 20 m/s. At the entrance to the test section, the bottom window contains a series of machined spanwise tripping grooves, which are located 165 mm (9~22 boundary layer heights) upstream of the SHSs whose purpose is to force early boundary layer transition to turbulence, as shown in prior studies (Liu & Katz 2013). The 152 mm long and 50 mm wide SHS is flush mounted on the same wall. The coordinate system is also shown, with x, y, and z denoting the streamwise, wall-normal, and spanwise direction, respectively, with x=0 coinciding with the leading edge of the SHS, all consistent with the coordinates used in the Introduction. The SHSs have been created on both porous stainless steel bases and non-porous aluminum bases, denoted as SHS_{Por} and SHS_{Al}, respectively. The SHS_{Por} is manufactured by spray-coating a mixture of a poly methyl methacrylate (PMMA) binder and fluorinated polyhedral oligomeric silsesquioxane (F-POSS) using procedures described in (Srinivasan *et al.* 2011). The reason for using a porous substrate as a base is to provide a means for continuously replenishing the micro-air pockets that are gouged away and entrained by the flow. A sample scanning electron micrograph (SEM) of the porous bases prior to spraying is shown in figure 1(b). They have a permeability of 200~700 (psid·ft^2/acfm/cp/inch) and porosity of 17~26%, as specified by the manufacturers. The size of particles forming the bases as seen in the SEM images (since the manufacturer does not provide them) varies from 20 to 40 μm. The porous bases are tightly glued to six 6.4×6.4 mm^2 support legs and 5.2 mm wide edges, leaving ~70% of their underside exposed to an air chamber. This chamber is connected through valves to a compressor and a vacuum pump, allowing us to set it at desired pressures P_1. The pressure in the test section, P_2, is also controled by connecting the same compressor and vacumm pump to an air-water interface located in a chamber well above the test section (Gopalan & Katz 2000). The pressure difference across the porous wall, $\Delta P=P_2-P_1$ can be varied and is monitored by a pressure transducer.

The SHS_{Al} is manufactured by polishing the Al manually, and then etching it in hydrochloric acid, boiling it in water and coating with (heptadecafluoro-1,1,2,2-tetrahydrodecyl) trichlorosilane using vapor deposition. Further details are provided in Yang *et al.* (2011). Two different subtypes of SHS_{Al} surfaces are involved in this study. In the first, surface polishing is performed in random directions, and the resulting surface is denoted as SHS_{Alr}. In the second, denoted as SHS_{Alx}, the polishing is intentionally aligned in the x direction, and as a result, streamwise grooves are formed with typical spacing of about 110 μm, while the remaining chemical treatment and silanization procedure is kept the same. A sample SEM image of SHS_{Alx} is shown in figure 1(c). For these samples, ΔP is used to denote the pressure difference between P_2 and atmosphere pressure when we examine effects of compressing the air layer on the skin friction. To characterize the SHSs before the water tunnel tests, the static contact angle and sliding angles of water droplets on the surface are measured. The contact angles are calculated by recording images of static ~4 mm (~270 μL) water droplets situated on the SHSs, e.g., figure 1(d). The sliding angles are determined by slowly tilting the SHSs until the droplets start moving and rolling off of the surface.

The optical setup for performing high resolution velocity measurements is illustrated in figure 2(a). To fully resolve the flow in the inner part of the boundary layer, we have opted to use in-line digital holographic microscopy (DHM). Since we cannot record holograms through the porous SHSs, we have developed a new approach to record DHM data in 'deep' samples, as described in detail by Ling & Katz (2014). In-line holographic reconstruction creates twin 3D images located symmetrically on both sides of the hologram plane. Thus, placing the hologram plane in the middle of the sample volume (i.e., to sustain submicron resolution), particles located on one side of the hologram will be reconstructed on both sides, 'mixing' them. To overcome this problem, we record a pair of holograms whose planes are separated by ~50 μm from each other. The real particle fields of both images coincide, whereas the virtual/twin ones are separated by twice the distance between planes. The software and procedures are discussed in detail and demonstrated in Ling & Katz (2014). The light source is an Nd-YAG laser (532 nm). Since very little energy is required for inline DHM, only light reflected from an uncoated flat glass surface is used. The beam is spatially filtered, expanded and collimated to

5 mm diameter before illuminating the sample volume. The flow is seeded locally with 2 μm silver-coated glass particles. To minimize the effect of injection on the flow, the particles are injected at a low a speed of less than $0.08U_m$ from twenty-five evenly-distributed 100 μm holes located ≥100 mm (1000 injector diameters) upstream of the sample volume. The light scattered by these particles interferes with the remainder of the collimated beam to form the inline hologram. An 8× infinity-corrected, long working distance microscope objective magnifies the images, while focusing on the selected hologram planes. A cube beam splitter directs the images to two interline transfer digital cameras (Imperx ICL-B6640, 4400×6600 pixels, 5.5 μm/pixel) generating a pair of holograms whose focal planes are located about 2 mm away from the center of the test section, separated by 50 μm, and at x=70 mm, as shown in figure 2(a). They have calibrated spatial resolutions of 0.677 and 0.685 μm/pixel. The total sample area cross section is 4.4×2.4 mm^2 (x×y) and the total depth of the interrogated volume extends to 3.2 mm in the z direction for most cases. However, as discussed below, this domain is divided into multiple sample volumes, which are interrogated separately.

High-speed digital holography has been used to monitor the air layer interface and measure the entrainment rate of air from the SHS_{Por}, as sketched in figure 2(b). Here, the light source is a Q-switched Nd:YLF laser (523 nm) whose output is expanded and collimated to a 10 mm diameter beam. The holograms are recorded by a high-speed camera (PCO.Dimax HD) at 20 000 frames per second and at a resolution of 11 μm/pixel. The sample volume is centered at x=70 mm, and has a streamwise length of 9.5 mm, a wall-normal height of 2.5 mm, and a depth of 50 mm, the latter covering the entire depth of the water tunnel. Three sample high speed movies of original holograms of the air layer on the SHS_{Por} for U_m varying between 2 to 6 m/s, and ΔP varying between −4.0 to 12 kPa, are available in the online supplementary data. They provide direct confirmation that an air layer or plastron (Shirtcliffe *et al.* 2011) is indeed attached to the SHS_{Por}, and this interface fluctuates at increasing surface speeds with increasing U_m. To measure the size distribution of bubbles and their cumulative volume, the holograms are reconstructed every 100 μm. The 3D intensity field is subsequently collapsed into a single plane, where each pixel has the minimum intensity (darkest) over the entire depth. The collapsed image is thresholded and segmented to identify each bubble and obtain its size. The flux of bubbles is calculated by dividing the cumulative volume of all the bubbles in the sample volume, averaged over eight realizations, by the time that is required for them to pass through the sample volume. This time is estimated by dividing the length of the sample area by the height-dependent mean streamwise velocity of the fluid. This flux is used for estimating the rate of bubbles entrainment from the upstream 70 mm of the porous surface (3,500 mm^2). This estimate is smaller than the actual entrainment rate since some of the bubbles might be lifted to elevations located above the sample volume. However, by tracking the vertical bubble flux at different elevations and determining that it is negligible at the top of the sample volume, and by insuring that buoyancy alone is insufficient to lift the bubbles away from the field of view, the overwhelming majority of the bubbles entrained from the wall remain inside the sample volume. It should also be noted that without the air layer, there are no freestream bubbles with resolvable sizes near the bottom wall. The entrainment rate of the bubbles is then divided by the surface area and U_m to obtain the dimensionless, spatially and time averaged air velocity U^*_{air}. As expected, U^*_{air} increases with increasing U_m and decreasing ΔP, as shown in figure 3(a). For U_m=2.0 m/s (Re_τ=1408, as discussed later), U^*_{air} is essentially zero, i.e., the boundary layer shear stresses fall below the threshold required for entraining the air, but it increases to 1.5×10^{-10} at U_m=6.0 m/s and ΔP=−4.0 kPa. Sample ensemble-averaged size distributions of entrained bubbles are shown in figure 3(b). The results for U_m=2.0 m/s is not included since it is zero, but the rest demonstrate that the number of ‘large’ bubbles (>50 μm) increases with entrainment rate. However, the high-speed movies confirm that both the air layer and the steady entrainment of bubbles is maintained on the SHS_{Por} for more than four hours for the entire current range of U_m and ΔP, presumably because of the continuous replenishment of the plastron by air under the porous surface. The persistence of the entrainment for $0<\Delta P<20$ kPa indicates that the capillary forces are sufficient for overcoming the air layer suppression by the higher pressure in the test section. To remove the air layer in some experiments, the entire space under the porous base has to be filled with water. We have not tried pressures exceeding ΔP=20 kPa, fearing that it might damage the substrate.

The optical setup of figure 2(a) with the same magnification and sample area is used to evaluate and quantify the topographies of each SHS_{Por} and SHS_{AIr}. The local roughness height $h(x)$ is extracted by selecting a certain threshold and tracking the cross section of the projection of the surface. In figure 4(a), we present sample histograms of $h(x)$ for one SHS_{Por} and the SHS_{AIr} along with their corresponding holograms. The $h(x)$ is demarcated by the dotted lines in the insets of figure 4(a). As the histogram appears to be nearly Gaussian, we characterize the roughness height using the root-mean-square (rms) value of $h(x)$, and denote it as k_{rms}. For the present measurements, the magnitude of k_{rms} of the SHS$_{\text{Por}}$ ranges from 4.8 to 20.4 μm and that of the SHS$_{\text{Alr}}$ is 10.9 μm, with an uncertainty of about 1 μm. Figure 4(b) shows the cumulative distributions of $h(x)$ for five values of k_{rms}. We have also noticed that after running for more than four hours at U_m=6.0 m/s, the roughness height of the SHS$_{\text{Por}}$ decreases significantly, presumably due to mechanical degradation and entrainment of the polymeric-sprayed material. Values measured at the end of the experiments are used in subsequent discussions. This phenomenon does not occur at U_m=2.0 m/s or for the SHS$_{\text{Al}}$. The holograms are not suitable for characterizing the roughness height of SHS$_{\text{Alx}}$ since the roughness elements are not projected outward. Therefore, for SHS$_{\text{Alx}}$, we utilize laser interferometer with a resolution of about 1 μm in both x and z directions to measure the height distribution. The values of k_{rms} of the SHS$_{\text{Alx}}$ in the flow measurement area (x=70 mm) is 8.9 μm. To obtain an estimate of the uncertainty in k_{rms}, the laser interferometer has also been applied to obtain independent measurements of roughness for one of the SHS$_{\text{Por}}$ and the SHS$_{\text{Alr}}$. The results give k_{rms} values that are lower by 10~20% than those obtained from the holograms. Hence, this difference is used as a rough estimate of our uncertainty in roughness measurements. The location of y=0 is selected as the mean roughness height, consistent with previous rough walls studies (Brzek *et al.* 2008, Chan *et al.* 2015). It is indicated by solid lines in the insets of figure 4(a). Selecting a different origin within the roughness domain has negligible effect on the mean profile in the log region. To minimize the potential effects of form drag, the wall friction and slip velocity are calculated at the top of the roughness, which is selected as the elevation where the cumulative distribution of $h(x)$ reaches 95%, namely $y=2k_{rms}$. The location of this elevation is indicated by the dashed lines in the insets of figure 4(a) and in figure 4(b). While one could also define the top of the roughness as the point where the cumulative distribution of $h(x)$ reaches e.g., 90% or 99%, the impact of this choice on the uncertainties in slip velocity and wall friction is discussed and accounted for later in the Results section.

To calculate the velocity field from the high resolution holograms obtained from the setup described in figure 2(a), the following data analysis procedures are employed. First, to reconstruct only the real particle images, we use a phase based reconstruction (Denis *et al.* 2005, Ling & Katz 2014), which involves a spatial convolution of both the intensity and phase (complex amplitude) distribution in (one of) the hologram plane with the Rayleigh-Sommerfeld kernel (Katz & Sheng 2010). The phase distribution is estimated iteratively by propagating the wave field back and forth between the two hologram planes using diffraction theory (Denis, Fournier et al. 2005). This phase based reconstruction is performed every 13 μm in depth to generate a series of closely spaced planes containing real images. Then, following Sheng *et al.* (2008) and Talapatra & Katz (2013), the 3D fields are segmented to generate the spatial distribution of particles, followed by particle tracking to match particle traces in the hologram pairs. Between 6000 to 10 000 particles pairs are typically matched in each of the 4.4×2.4×3.2 mm^3 (x×y×z) sample volumes. Matching involves seven criteria, including similarity of particle size, shape and intensity, as well as smoothness of the velocity field and agreement with guess 2D vectors generated using standard particle image velocimetry (PIV) cross-correlations of images created by compressing the entire volume into a plane. Symbols u, v, and w are used to denote the instantaneously velocity components in x, y, and z directions respectively. The magnitudes of u and v are calculated from the in-plane centroids of the particles and w is calculated based on locations of minimum intensity within the elongated traces of particle in the spanwise direction. The accuracy of w is lower compared to u and v but could be improved by locating the center of the particles using edge detection (Talapatra & Katz 2013) and correlations among the elongated traces (Ling & Katz 2014). However, as the focus of this paper is on the distributions of u and v, additional effort is not invested in improving the accuracy of w. The sample volume is divided into multiple small windows with a size of $10\delta_\nu \times 1\delta_\nu \times 10\delta_\nu$ (x×y×z) for U_m=2 m/s, and $20\delta_\nu \times 1\delta_\nu \times 20\delta_\nu$ (x×y×z) for U_m=6 m/s. Only the windows containing particles are included in the statistical analysis for each volume. More than 1000 instantaneous velocity fields are processed and ensemble-averaged locally for each window to obtain the mean (dented as U and V) and the corresponding Reynolds normal and shear stress components, $<u'u'>$, $<v'v'>$ and $<u'v'>$. Results are then spatially averaged in the x and z directions to obtain data that are not dependent on the local roughness patterns. Spatially averaged values are denoted with an over bar, e.g., $\overline{U}$, $\overline{<u'v'>}$, and etc.

For SHS$_{\text{Por}}$, the measurement domain starts from y=0, and the first data point included in this paper is located at $y=\delta_\nu$. This point is located below the tip of the roughness elements. For SHS$_{\text{Alr}}$, the measurement domain starts from $y=k_{rms}$ and the first data point is located at $y=k_{rms}+\delta_\nu\approx 2k_{rms}$. For SHS$_{\text{Alx}}$, we cannot examine the space between the roughness elements. Therefore, the location of y=0 can only be estimated based on observed particles attached to the surface. Hence, the first data point is located at $y \approx 2k_{rms}+1\delta_\nu$. The values of the mean spatially averaged viscous stress, τ^μ, are calculated using $\tau^\mu = \mu\,\partial\overline{U}/\partial y$, where $\mu = 1\times10^{-3}$ $kg/m/s$. Since the mean velocity profiles for the smooth walls, the SHS_{Por} with $k_{rms} \le \delta_\nu$, and the SHS_{AIr} are nearly linear at $y \le 5\delta_\nu$, the values for $y<3\delta_\nu$ are calculated by linearly fitting the mean velocity profiles based on the $y \le 5\delta_\nu$ data. However, for the SHSs with $k_{rms}>\delta_\nu$, the mean profiles are not linear at $y \le 5\delta_\nu$. Thus, τ^μ at $y=\delta_\nu$ (first point) is not available, and so 2nd order finite differencing is used for $y=2\delta_\nu$, and 5 points are used for higher elevations. The total stress $\tau_t=\tau^\mu+\tau^R$ is determined by adding τ^μ and the spatially averaged Reynolds shear stress, $\tau^R = -\rho\overline{<u'v'>}$, where $\rho=1\times10^3$ kg/m^3. The wall viscous stress $\tau_w{}^\mu$, wall Reynolds shear stress $\tau_w{}^R$ and total wall friction τ_w are determined from the corresponding stresses at $y=0$ for smooth walls, $y=2k_{rms}$ for SHS_{Por} and SHS_{AIr}, and at $y=2k_{rms}+1\delta_\nu$ for SHS_{AIx}. To estimate the slip velocity, we calculate the mean and spatially averaged velocity at $y=2k_{rms}$, and denote it as $\overline{U}_s$. The associated uncertainties are discussed later on.

High resolution velocity measurements have been performed for 20 cases, and results for 13 of them are included in this paper. As listed in table 1, they include SHS_{Por}, SHS_{Al}, and smooth walls, with U_m varying from 2 to 6 m/s, pressure differences in the range $-0.3 \le \Delta P \le 20$ kPa, rms roughness height varying between $4.8 \le k_{rms} \le 20.4$ μm, and two streamwise locations. For control measurements above smooth walls, the SHSs are exchanged with smooth PVC bases and the measurement locations are kept identical as those of the SHSs. Table 1 also provides results of contact and sliding angle measurements performed before each experiment, which are denoted as *CA* and *SA*, respectively. The contact angle after the experiment and exposing the wall to air is also provided for some of the cases (in parenthesis). Each flow measurement is started after running the facility continuously at a particular condition for at least one hour. Each data acquisition lasts about two hours. Also listed in table 1 are the $\tau_w{}^\mu$, $\tau_w{}^R$, τ_w, $\overline{U}_s$, and their associated uncertainties. The values of $u_\tau=(\tau_w/\rho)^{1/2}$ and δ_ν based on τ_w are provided in table 1. These values are used for the inner scaling. In the rest of the paper, a superscript $^+$ is used for quantities that are normalized by u_τ and δ_ν, a subscript $_0$ for quantities measured above the smooth wall (the baseline), and the combination of the superscript $^+$ and subscript $_0$ for quantities normalized by $u_{\tau0}$ and $\delta_{\nu0}$. For all cases, in addition to τ_w, we also estimate the wall friction by a logarithmic fit to the mean velocity profile in the regions where values of $y\,\partial\overline{U}/\partial y$ are nearly unchanged, which fall in the range of $80\delta_\nu<y<180\delta_\nu$ for cases #1 to #6 and #13, $50\delta_\nu<y<180\delta_\nu$ for cases #7 to #9, and $50\delta_\nu<y<350\delta_\nu$ for cases #10 to #12. Results, denoted as $\tau_w{}^{Log}$, along with the maximum value of the total stress across the entire boundary layer, denoted as $\tau_t{}^{max}$, are also listed in table 1. There are mismatches between the log layer based estimate of wall stress and the directly measured value. Implications of these findings are discussed later in this paper.

Because the high resolution measurements only cover the inner part of the turbulent boundary layers, two-dimensional (2D) PIV has also been used to obtain the entire boundary profile, including the missing wake region, but at lower magnification (5.4 μm/pixel), and larger sample area (36×24 mm^2, $x\times y$). The centers of the sample areas (x=70 mm) coincide with those of high resolution measurements. These 2D PIV measurements have also been performed after running at a particular experimental condition continuously for one hour. Data acquisitions typically last for 30 minutes, during which more than 250 pairs of images are captured. Standard PIV cross-correlations using in-house software (Roth & Katz 2001) with window size of $64\delta_\nu\times16\delta_\nu$ ($x\times y$) for U_m=2 m/s, $128\delta_\nu\times32\delta_\nu$ ($x\times y$) for U_m=6 m/s and 50% overlap are used to calculate the velocity, resulting in a characteristic grid spacing of $32\delta_\nu\times8\delta_\nu$ ($x\times y$) for U_m=2 m/s and $64\delta_\nu\times16\delta_\nu$ ($x\times y$) for U_m=6 m/s. The boundary layer thicknesses, δ_{99}, as listed in table 1, are based on the elevation where 99% of the maximum velocity (U_0) is reached. Note that U_0 is slightly higher (typically by 8~12%) than U_m owing to the boundary layer induced blockage. As is evident, unlike the wall total stress, the effects of the SHSs on δ_{99} are small, possibly since the present fetch (4-9δ_{99}) is limited. The magnitudes of the drag reduction are defined as $DR=(\tau_{w0}-\tau_w)/\tau_{w0}$, where τ_{w0} is the value obtained for the smooth wall at the same U_m and (very similar) δ_{99}. To calculate the velocity deficit or increase in the log region, ΔU^+, the mean velocity profile is fitted with $\overline{U}^+ = (1/\kappa)\ln y^+ + \Delta U^+ + B_0$, where B_0 is the value obtained for the corresponding smooth wall. For subsequent discussion, values of $Re_\delta=U_0\delta_{99}/\nu$, $Re_\tau=u_\tau\delta_{99}/\nu$, $k_{rms}{}^+$, ΔU^+, $\overline{U}_s^+$, and DR are also included in table 1. Note that when normalized, $\overline{U}_s^+ = \overline{\lambda}_x^+$ for the cases where $\tau_w=\tau_w{}^\mu$, and $\overline{U}_s^+ < \overline{\lambda}_x^+$ for the cases where $\tau_w>\tau_w{}^\mu$ or $\tau_w{}^R>0$.

Two facts need to be considered when comparing the presently measured wall friction to that of much larger surfaces. First, there is a relative short distance (4-9δ_{99}) from the beginning of the SHSs to the sample area. Prior studies have reported an overshot of the wall friction after transitioning from a smooth to a rough wall and an undershot after transitioning from a rough to a smooth wall (Antonia & Luxton 1971). Further downstream, the wall friction adjusts to the new boundary condition after a distance that increases with decreasing δ_{99}/k. For example, a relatively short distance of 2~3δ_{99} is required for δ_{99}/k>1,000 (Saito & Pullin 2014), and a much longer distance of about 30δ_{99} is needed for δ_{99}/k<25 (Lee & Sung 2007). To the best of our knowledge, there are no experimental or numerical data for the transition from a smooth wall to a SHS. If the roughness effects are dominant (as will be shown to occur in some cases), one would expect a rather quick transition considering δ_{99}/k>100 for current samples. For cases of skin friction reduction, we have no basis for comparison. Consequently, we have performed additional measurements in a sample area located at x=35 mm (3.9δ_{99}) for the same conditions (U_m and ΔP) as these performed at x=70 mm (7.7δ_{99}) for case #5, and denote it as case #13 (table 1). Second, without the plastron, the current SHSs fall in the transitionally-rough to rough regimes (Schultz & Flack 2007), and form drag might affect the total stress at the spatially averaged top of the roughness elements. However, based on computational results found in (Chan *et al.* 2015), for a transitionally rough surface with k^+=10, the total stress normalized by the wall friction near the roughness tip increases from about 0.87 to 0.97 as δ_{99}/k increases from 9 to 25, with the viscous stress contributing about 60% in both cases. In the current study, considering that δ_{99}/k_{rms}>100 and k_{rms}^+<5, it is reasonable to expect that the total stress near the roughness tip represents the wall friction.

3. Results

3.1. *Mean flow quantities on smooth walls (baseline)*

Data for smooth walls have been obtained as a baseline for comparison with the SHSs at the same location and free stream flow conditions. Wall stress results for the four different values of Re_δ are summarized in table 1 (Cases #1, #7, #10, #11). Due to differences in the inlet boundary conditions at the entrance to the test section imposed in the settling chamber, we achieve two different boundary layer characteristics for each of the present speeds, i.e., δ_{99}=9.1 mm and 16.6 mm for U_m=2.0 m/s, as well as 7.4 mm and 18.8 mm for U_m=5.5-5.9 m/s, with the corresponding changes to τ_w and δ_ν. The latter falls in the $10\leq\delta_\nu\leq12$ μm range for the low speed measurements and $\delta_\nu\approx4.4$ μm for the high speed tests. The corresponding values of Re_τ vary from 863 to 4287. In all cases, the differences between the measured wall stress and predictions based on fits to the log layer profiles are less than 2%, further emphasizing the validity of the procedures used for calculating the stresses in this study. Figure 5 shows that all the four normalized mean velocity profiles obtained using DHM collapse onto the classical law of the wall, namely $\overline{U}^+=y^+$ for the viscous sublayers ($y^+\leq5$) and the familiar log-law $\overline{U}^+=(1/\kappa)\ln y^+ + 5.2$ for the log layers. The 2D PIV data coincides with the DHM results in the log region, but extends to the wake and free stream flow. The DHM based velocity fluctuations for the smooth walls are plotted in figure 6. As expected, $\overline{<u'u'>}$ peaks in the y^+=12 to 20 range, reaching values of 7 to 8, consistent with previously published data (Sheng *et al.* 2009). In the log layer $\overline{<u'u'>}$ increases with Re_τ, in agreement with Smits (2011). The values of $\overline{<v'v'>}$ reach a maximum of 1.6 to 1.9 at y^+=50 to 100, again consistent with expectations. Figure 7 presents profiles of the viscous and the Reynolds shear stresses along with the total stress. These results are also consistent with expectations, with the viscous stress decreasing monotonically and Reynolds shear stress increasing with elevation for y^+<70, and then decreasing. For y^+>70, the Reynolds shear stresses increases with increasing Re_τ. The total stress remains nearly constant up to about y^+=20, and then starts decreasing at a rate that decreases with increasing Re_τ.

3.2. *Effect of k_{rms}^+ and Re_τ on the mean flow quantities for the SHS_{Por} and SHS_{Alr}*

Profiles of viscous, Reynolds and total shear stresses for all the porous based sprayed surfaces, the etched Aluminum surface, and the smooth walls are shown in figures 8, 9 and 10, respectively. In each plot, the SHS_{Por} results are presented using solid symbols, the SHS_{Alr} data by crosses, and the smooth wall profiles by hollow symbols. The specific flow conditions corresponding to each of the symbols can be found in table 1.

The location of $y=2k_{rms}$ for each profile is marked by a short vertical line. Each profile is presented using two scales. In figures 8(a), 9(a), and 10(a), the results are scaled by the total wall stresses of the smooth walls for the same U_m and very similar δ_{99} in order to highlight the differences from the smooth wall behavior. In figures 8(b), 9(b), and 10(b), each profile is scaled by its own wall stress. Several trends are immediately evident. First, near the wall the viscous stresses for all the SHSs are lower than those of the corresponding smooth wall values (for the same U_m and δ_{99}). In the outer regions, the SHSs and smooth wall results collapse. The viscous stresses decrease systematically with increasing k_{rms}^+. The values of τ_w^μ/τ_w also decrease with increasing k_{rms}^+, but their magnitudes are inherently higher than the corresponding τ_w^μ/τ_{w0} for the cases with skin friction reduction (cases with $k_{rms}^+<1$), and lower than it when the total wall stress increases, i.e., for $k_{rms}^+=3.28$. As expected for all the SHSs, the viscous stresses decrease with distance from the wall. In contrast, near the wall, Reynolds shear stresses for all the SHSs are larger than those of the corresponding smooth walls results (figure 9). Moreover, they are always non-zero at $y=2k_{rms}$, and their magnitude increases with increasing k_{rms}^+. Results for $k_{rms}^+=1.71$ and 3.28 are much higher than the rest. The locations and values of Reynolds shear stress maxima also depend on k_{rms}^+. For $k_{rms}^+<1$, the peaks normalized by τ_{w0} have values and locations that are very close to those of the corresponding smooth walls. For $k_{rms}^+>1$, the magnitudes are distinctly higher. When the Reynolds stresses are normalized by their own τ_w, the differences between peak values and their locations decrease, but all the SHSs peaks are consistently larger than those of the smooth walls. The total stresses on the SHSs also depend strongly on k_{rms}^+. For all the $k_{rms}^+<1$ cases, $\tau_t/\tau_{w0}<1$ at $y=2k_{rms}$, indicating a reduction of drag by these surfaces. The reduction is mild, ~10% for the SHS_{Por}, and above 25% for the SHS_{Alr}. For the $k_{rms}^+=1.71$ case, τ_t/τ_{w0} ($y=2k_{rms}$) is very close to 1, but for $k_{rms}^+=3.28$, τ_t/τ_{w0} is already significantly larger than 1. Considering that for the latter case, τ_w^R is the primary contributor to the total stress, it is clear that the surface roughness dominates the total drag. With increasing rms values of roughness height, the SHSs switch from facilitating drag reduction when $k_{rms}^+<1$ to increasing the drag for larger k_{rms}^+. Similar trends are reported by Bidkar *et al.* (2014) based on force measurements of floating SHSs in a water tunnel. Their SHSs are generated by spray coating, cover a range of k_{rms}^+ ranging from 0.1 to 6, and show a maximum drag reduction of 30% for $k_{rms}^+<0.5$, and an increase in drag for $k_{rms}^+>1$.

For the SHS_{Por}, the values of τ_t^+ collapse at $10<y^+<30$, irrespective of roughness height (figure 10b). They increase slightly with distance from the wall for $y^+\leq 2k_{rms}^++5$, peaking with values of about 1.05, and then remain nearly constant until $y^+=30$, except for $k_{rms}^+=3.28$, for which the constant stress layer persists up to $y^+=300$. There is a persistent difference between the SHS_{Por} and the smooth wall results in the constant stress region, suggesting that SHS_{Por} boundary layers are under non-equilibrium conditions, with the wall stresses being lower than those at higher elevation, presumably since the outer layers have not 'relaxed' yet from the smooth wall conditions. This claim is supported by the figure 10(a), which shows that, for $k_{rms}^+<1$, i.e., the drag reduction cases, and at $5<y^+<10$, τ_t/τ_{w0} is nearly matched with the smooth wall values. The trends are very different for the rougher walls, presumably since turbulent mixing speeds up the momentum exchange between the inner and outer regions. The non-equilibrium conditions appear to be more severe for the SHS_{Alr}, for which the drag reduction is significantly higher. Yet, its peak τ_t/τ_{w0} is nearly the same as those of the smooth wall and SHS_{Por} at $y^+=6$, but it decreases sharply closer to the wall. At $6<y^+<100$, τ_t/τ_{w0} of the SHS_{Alr} is lower than that of the other surfaces, but appears to collapse with the results for similar Reynolds numbers at higher elevations. Due to the lower wall stress, values of τ_t^+ of the SHS_{Alr} are much higher than the others in the inner part of the boundary layer, but the difference decreases in the outer regions. The mismatch between τ_w^{Log} and τ_w for all the SHSs is another way to show non-equilibrium conditions. As listed in table 1, for all the drag reduction cases, the values of τ_w^{Log} are larger than the corresponding τ_w, and are very close to those of τ_{w0} for the same Reynolds number. This trend implies that the log region has not adjusted yet to the lower skin friction. Conversely, for the cases showing drag increase, τ_w^{Log} is noticeably larger than τ_{w0}, consistent with the previously argued effect of roughness-induced increase in wall-normal momentum exchange.

Using the same symbols, figure 11 shows the mean velocity profiles for the SHS_{Por}, SHS_{Alr} and the smooth walls scaled by their own inner units. The inset highlights the near wall velocity profiles using a linear scale (and the axes switched), which allows direct comparison to linear least square fits. It confirms that for $k_{rms}^+<1$, the inner profiles are nearly linear when $y^+\leq 5$, but are slightly curved for $k_{rms}^+>1$. For all the $k_{rms}^+<1$, or drag reduction SHS cases, the mean velocity is higher than that of the smooth wall at all elevations, consistent with the numerical results by Min & Kim (2004) and experimental measurements by Woolford *et al.* (2009). The upward shift in the log region is smaller than that occurring near the wall. There are two possible reasons for this difference. First, it might be influenced by the previously discussed non-equilibrium condition, i.e., that the log layer mean momentum has only partially adjusted to the lower wall friction. However, these differences have also been observed in DNS results obtained for equilibrium conditions, which Min & Kim (2004) attribute to spanwise slip, which increases the skin friction by contributing to the generation of streamwise vortices. In simulations prescribing only streamwise slip, i.e., $\lambda_x \neq 0$ and $\lambda_z=0$, the upward shift in the velocity profile is uniform. Conversely, for the drag increase case ($k_{rms}^+=3.28$), the log layer mean momentum is lower than that of the smooth wall, and the entire profile resembles that measured over rough wall, which is characterized with lower mean velocity gradients in the inner part of the boundary layer (Chan *et al.* 2015). For $k_{rms}^+=1.71$, the profile appears to be a transition from drag reduction to drag increase, with the inner region resembling a rough wall and a mild slope, and the outer region in the process of crossing from the momentum increase to momentum decrease regimes.

Figures 12(a) and (b) present distributions of $\overline{<u'u'>}$ and $\overline{<v'v'>}$, respectively. For all non-smooth wall cases, regardless of the magnitude of k_{rms}^+, both $\overline{<u'u'>}$ and $\overline{<v'v'>}$ are significant in the vicinity of the roughness tips, and remain higher than the smooth wall values at $y^+<10$. These trends are consistent with reported numerical results for SHSs (Busse & Sandham 2012). For the drag reduction cases ($k_{rms}^+<1$), $\overline{<u'u'>}^+$ increases with distance from the wall in the inner layer, peaks at $6<y^+\leq 10$, and then decreases at higher elevations, where it nearly collapses to the corresponding smooth wall data at $y^+>20$. The peak values are slightly larger than those of the smooth wall by about 5%, and are located closer to the wall. While the shift in location is consistent with the numerical results, the higher magnitude is not (Min & Kim 2004). There are several likely reasons for the discrepancy, such as roughness effects, motion of the air-water interface, spatial non-uniformity, and even the non-equilibrium conditions. It should be noted that the actual magnitudes of the $\overline{<u'u'>}^+$ peaks for all the drag reduction cases are slightly lower than those of the corresponding smooth walls, i.e their magnitude decreases, scaled using the smooth wall shear stress. Trends are quite different for the drag increase case ($k_{rms}^+=3.28$), for which $\overline{<u'u'>}^+$ flattens at $y^+<5$, and after having a broad maximum centered around $y^+\sim 9$, it decreases but remains higher than that of the corresponding smooth walls. While previously published trends for transitionally rough walls show that in the inner region $\overline{<u'u'>}^+$ can be higher or smaller than that of the smooth wall (Chan *et al.* 2015), the present trends for the log layer are inconsistent with the expected collapse to the smooth wall data (Hong *et al.* 2011, Jimenez 2004). The non-equilibrium condition appears to be a primary cause for this difference. Indeed, rescaling the $\overline{<u'u'>}^+$ profile based on τ_w^{Log} substantially reduces the difference from the smooth wall results, as shown in figure 13(a). Furthermore, simulations of the transition from a smooth to a fully rough surface show overshoots of $\overline{<u'u'>}^+$ in the log region (Saito & Pullin 2014). For the $k_{rms}^+=1.71$ case, at $y^+<5$, $\overline{<u'u'>}^+$ appears to have values and trends falling between those of the skin friction reduction and increase, but the broad peak appears at a lower elevation and has a lower magnitude than both. In the outer region, trends are similar to that of the $\mathrm{SHS_{Por}}$ for the same Reynolds number.

For all the SHSs, the profiles of $\overline{<v'v'>}^+$ have maximums in the $10<y^+<50$ range, closer to the wall than the smooth wall peaks. At $y^+>50$, for the cases with mild drag reduction ($k_{rms}^+<1$) and $k_{rms}^+=1.71$, the values of $\overline{<v'v'>}^+$ remain only slightly higher than those of the corresponding smooth wall. The difference is bigger for the $\mathrm{SHS_{Alr}}$, which causes more than 25% drag reduction. Conversely, for the drag increase case ($k_{rms}^+=3.28$), the values of $\overline{<v'v'>}^+$ in the inner part of the boundary layer are substantially higher than those of the smooth wall. This difference diminishes but does not vanish in the log layer. Such an overshot of the peak value of $\overline{<v'v'>}^+$ has been reported before for a boundary layer transitioning from a smooth to a rough wall, based on numerical simulations performed by Lee & Sung (2007) and by Saito & Pullin (2014). Both indicate that the elevated values decay slowly, e.g., for more than 500 momentum thicknesses in the former study. When the $\overline{<v'v'>}^+$ profiles are re-normalized based τ_w^{Log}, as shown in figure 13(b), the SHS profiles collapse to the smooth wall values at $y^+>20$ for $k_{rms}^+<2$ and at $y^+>100$ for the drag increase case ($k_{rms}^+=3.28$). But the differences in the inner part of the boundary layer persist, especially for the drag increase case.

3.3 *Effects of groove alignment, streamwise distance, and pressure on the stress profiles*

Groove Alignment: The effects of the surface geometry are examined by comparing the viscous, Reynolds and total shear stresses of the $\mathrm{SHS}_{\mathrm{Alr}}$ (random polish) and $\mathrm{SHS}_{\mathrm{Alx}}$ (streamwise polish/grooves) at the same location, and for the same Reynolds number, ΔP, and $k_{rms}{}^{+}$ (table 1), as shown in figure 14. Both surfaces reduce the wall friction by more than 20%. Although the magnitudes of the near wall stresses are different, this difference is pretty much limited to the near wall region, and the profiles nearly collapse onto each other at higher elevations. At $y^{+}<5$, both the viscous and Reynolds stresses above the $\mathrm{SHS}_{\mathrm{Alx}}$ are lower than those of $\mathrm{SHS}_{\mathrm{Alr}}$, indicating that the axially aligned grooves are more effective in reducing drag. Accordingly, table 1 shows that the slip velocity on the $\mathrm{SHS}_{\mathrm{Alx}}$ is higher than that of $\mathrm{SHS}_{\mathrm{Alr}}$. As both k_{rms} and contact angles are very similar, this difference might be associated with geometric differences, namely the ~110 μm (~$8.5\delta_{\nu}$) spaced streamwise grooves. Considering that the deeper ($5\sim15\delta_{\nu}$) streamwise riblets have already been shown to reduce drag in turbulent boundary layers over rigid walls, e.g., by 10% when the space of grooves is $15\delta_{\nu}$ (Garcia-Mayoral & Jimenez 2011), the groove alignment seems to play a role in the SHSs as well.

Streamwise Distance: The effects of streamwise distance from the transition between smooth to SHS distance has been evaluated by comparing the shear stresses on the $\mathrm{SHS}_{\mathrm{Alx}}$ at two locations, $x=3.9\delta_{99}$ and $7.7\delta_{99}$, the latter being the location of most of the present tests. Several trends can be observed from the results presented in figure 15. Except for the first point, where results are essentially identical, the total stress at $x=3.9\delta_{99}$ and $y^{+}<40$ is slightly higher than that further downstream, but the difference between them diminishes at higher elevations. Trends of the two contributors to this total stress differ. At $y^{+}<8$, the viscous stress at $x=3.9\delta_{99}$ is lower than that further downstream, but the profiles completely collapse at higher elevations. Conversely, the Reynolds shear stress at $x=3.9\delta_{99}$ is higher, and the difference between them slowly diminishes with increasing elevation, becoming very small at $y^{+}>40$. For both the viscous and Reynolds shear stresses, the profiles at $x=3.9\delta_{99}$ do not appear to be a transition between the smooth wall and the more developed SHS further downstream. Overshoot in drag at the transition from smooth to rough walls (Saito & Pullin 2014), and undershoots at the transition from rough to smooth walls (Antonia & Luxton 1971) have been seen before, and it is possible that the present differences are associated with similar transitional changes. This comparison also provides an upper limit for the effect of such transitional changes on the total stress measured at $x=7.7\delta_{99}$ for most of the present data.

Facility Pressure: The effects of ΔP are studied by comparing the stress profiles for the same $\mathrm{SHS}_{\mathrm{Por}}$ and the same $\mathrm{SHS}_{\mathrm{Alx}}$ under considerably different values of ΔP. For the porous surfaces, the sign of ΔP indicates the direction of airflow across the substrate, while for the $\mathrm{SHS}_{\mathrm{Alx}}$, a sufficiently high ΔP is expected to suppress the plastron that forms across the texture. For the latter, to make results meaningful, the pressure needs to be normalized by the surface tension, e.g., by σ/k_{rms}. For the most of the porous surface tests, $-0.08\leq\Delta P k_{rms}/\sigma\leq-0.02$, i.e., there is very slow air replenishment. Figure 16(a) compares the resulting profiles to those with $\Delta P k_{rms}/\sigma=1.33$ i.e., when air replenishment is suppressed, while the pressure difference is of the same order as the surface tension. As is evident, changing ΔP does not have a detectable effect on the viscous stress, and slightly increases the Reynolds stress, resulting in a slight increase in the total stress, while maintaining the drag reduction. It appears that under such pressure differences, the capillary forces are sufficient to maintain the air layer, as the holograms clearly show. In fact, under similar pressures, the drag reduction can only be suppressed by filling the chamber under the porous surface with water, and forcing it through the porous walls by the pressure difference. After doing this, the SHS surface is no longer super-hydrophobic, even after drying it. As for the etched aluminum SHSs, figure 16(b) compares the stress profiles for $\Delta P k_{rms}/\sigma=0.49$ and 2.47. As is evident and expected, suppressing the air layer causes a significant increase in the Reynolds and total stresses, and decreases the viscous stress in the inner part of the boundary layer. Both trends are consistent with an increase in the "effective" roughness height. Yet, the skin friction is still significantly lower than that of the smooth wall. Accordingly, the mean velocity profile at higher ΔP is less upward shifted (not shown). The increasing role of the roughness with increasing ΔP can also be observed from the distributions of the normal stresses shown in figure 16(c). Both the magnitudes of $\overline{<u'u'>}_{0}^{+}$ and $\overline{<v'v'>}_{0}^{+}$ increases with ΔP over the entire inner part of the boundary layer, consistent with the trends presented in figures 12 and 13.

4. Discussion and Conclusions

In this study, digital holographic microscopy is used for characterizing the profiles of mean velocity, viscous and Reynolds shear stresses, as well as turbulence level in the inner part of turbulent boundary layers over several super-hydrophobic surfaces. Two types of SHSs are involved, namely $\mathrm{SHS_{Por}}$ generated by sprayed coating hydrophobic material on porous bases, and $\mathrm{SHS_{Al}}$ created by using vapor deposition to coat etched solid aluminum bases. The magnitudes of Re_τ range from 693 to 4496, and k_{rms}^+ varies from 0.43 to 3.28. Experiments are also repeated at different streamwise locations and ambient pressures as well as aluminum surfaces that are either etched randomly or aligned in the streamwise direction. The wall shear stress is estimated from the sum of the viscous and Reynolds shear stress at the top of roughness elements, and the mean slip velocity is obtained from the mean profile at the same elevation.

The data shows that the near wall momentum transport involves a competition between two opposing effects, namely skin friction reduction by the SHSs, and an increase in Reynolds stresses with increasing roughness effects. Their relative significance depends on the values of k_{rms}^+. As k_{rms}^+ increases from 0.43 to 3.28, the near wall stresses transition from drag reduction, when the viscous stress dominates, to drag increase when the Reynolds shear stress is the primary contributor. For $k_{rms}^+<1$, the SHSs cause a reduction of drag, which introduces wall-normal gradients in the total stress, as well as an upward shift of the mean velocity profiles. In the log region, this upward shift is lower than that in the inner layer, a phenomenon observed before in both numerical simulations (e.g., Min & Kim 2004) and experimental measurements (e.g., Woolford *et al.* 2009). These changes are accompanied with increases in $\overline{<u'u'>}^+$ and $\overline{<v'v'>}^+$, the latter only slightly, in the inner part of the boundary layer, and a shift of their peaks closer to the wall. Roughness effects, motion of the air-water interface, spatial non-uniformity, and even the non-equilibrium conditions might play a role in the increase of the turbulence level. The non-equilibrium conditions associated with the limited length of the present samples cause a mismatch between the local wall stress and that estimated from a fit to the velocity profile in the log layer. This difference diminishes with increasing streamwise distance. When $k_{rms}^+=1.71$, it appears that there is a balance between drag reduction by the SHS and an increase by the roughness. For $k_{rms}^+=3.28$, the roughness becomes dominant, causing an increase in wall friction, a downward shift in the mean velocity profile, an increase in $\overline{<u'u'>}^+$ close to the wall, and a substantial increase in $\overline{<v'v'>}^+$, the latter being consistent with previous observations of the transition region from a smooth to a rough wall (Lee & Sung 2007). Consistent with prior experimental studies involving measurements of wall friction (Bidkar *et al.* 2014), it appears that the transition between drag increase to reduction occurs when k_{rms} is in the $1\le k_{rms}^+\le 2$ range.

Several other effects have also been observed. First, increasing the pressure in the facility to $\Delta P k_{rms}/\sigma>1$ appears to suppress the air layer, and presumably exposes the roughness elements to the liquid. Hence, the turbulence level and the shear stress in the inner part of the boundary layer increase. As one would expect, the effect of pressure on drag reduction cannot be ignored. Second, for the etched aluminum surfaces, aligning the surface groves in the streamwise direction causes higher drag reduction than a randomly polished surface. Finally, we conclude this paper by discussing the relationship between slip velocity, based on values measured at the top of the roughness, and the drag reduction for all the present SHSs. Figure 17 is a plot of DR vs. $\overline{U}_s^+$, where each case is represented by the symbols listed in table 1 and used throughout this paper. It also shows the theoretical predictions by Busse & Sandham (2012), based on equation (2) and the empirical function $F(\lambda_z^+)=16/(4+\lambda_z^+)-1$. The model results are provided for two relevant values of Re_τ, both for $\lambda_z=0$ and $\lambda_z=\lambda_x$. However, for the experimental data, λ_x^+ is replaced by $\overline{U}_s^+$ at the top of the roughness. That means that we assume that the present measurements are equivalent to a hypothetical case for which the air layer surface is aligned with the top of the roughness, and the viscous stress there is equal to the total stress. As discussed in Busse & Sandham (2012), the introduction of spanwise slip and an increase in Re_τ reduces the extent of drag reduction. The $\lambda_z=0$ case predictions agree with the DNS results of Park *et al.* (2013a) for an SHS consisting of long and broadly spaced streamwise grooves, which presumably involve limited spanwise slip. However, as is evident, except for the $\Delta P k_{rms}/\sigma=2.47$ test, all of the present cases that involve drag reduction fall close to the predicted values assuming $\lambda_z^+=\lambda_x^+$. Only three experimental cases deviate significantly from the predicted values, all of which involve an increasing role of roughness. Two of them are the $k_{rms}^+=1.71$ and 3.28 cases, and the third is the $\mathrm{SHS_{Alx}}$ with $\Delta P k_{rms}/\sigma=2.47$, namely when the plastron is partially suppressed (the drag is still lower than the smooth wall value) by increasing the pressure in the test facility. Hence, for situations where the roughness effect is not dominant, i.e., the Reynolds stress at the top of the roughness is much lower than the viscous stress, the present measurements confirm the theoretical relationship between drag reduction and slip length for a turbulent boundary layer over an SHS. To the best of our knowledge, the present study provides the first simultaneous direct measurement of both slip velocity and drag reduction, allowing such a comparison.

Acknowledgements

This research has been performed under the ONR MURI program on Passive and Active Friction Drag Reduction of Turbulent Flows over Super-Hydrophobic Surfaces led by S. Ceccio. The program officer is Ki-Han Kim. The authors also thank S. King and Y. Ronzhes for their assistance in setting up the experiments, and J. Wang for developing the GPU-based hologram reconstruction code.

REFERENCES

Aljallis E, Sarshar MA, Datla R, Sikka V, Jones A, Choi CH. 2013. Experimental study of skin friction drag reduction on superhydrophobic flat plates in high Reynolds number boundary layer flow. *Physics of Fluids* 25

Antonia RA, Luxton RE. 1971. Response of a Turbulent Boundary Layer to a Step Change in Surface Roughness .1. Smooth to Rough. *Journal of Fluid Mechanics* 48: 721-&

Bidkar RA, Leblanc L, Kulkarni AJ, Bahadur V, Ceccio SL, Perlin M. 2014. Skin-friction drag reduction in the turbulent regime using random-textured hydrophobic surfaces. *Physics of Fluids* 26

Brzek BG, Cal RB, Johansson G, Castillo L. 2008. Transitionally rough zero pressure gradient turbulent boundary layers. *Experiments in Fluids* 44: 115-24

Busse A, Sandham ND. 2012. Influence of an anisotropic slip-length boundary condition on turbulent channel flow. *Physics of Fluids* 24

Ceccio SL. 2010. Friction Drag Reduction of External Flows with Bubble and Gas Injection. *Annual Review of Fluid Mechanics* 42: 183-203

Chan L, MacDonald M, Chung D, Hutchins N, Ooi A. 2015. A systematic investigation of roughness height and wavelength in turbulent pipe flow in the transitionally rough regime. *Journal of Fluid Mechanics* 771

Charles H, Tom K, Paul K, Taylor J, Hodes M, et al. 2006. Turbulent Drag Reduction Using Superhydrophobic Surfaces In *3rd AIAA Flow Control Conference*: American Institute of Aeronautics and Astronautics

Choi H, Moin P, Kim J. 1993. Direct Numerical-Simulation of Turbulent-Flow over Riblets. *Journal of Fluid Mechanics* 255: 503-39

Daniello RJ, Waterhouse NE, Rothstein JP. 2009. Drag reduction in turbulent flows over superhydrophobic surfaces. *Physics of Fluids* 21

Dean RB. 1978. Reynolds-Number Dependence of Skin Friction and Other Bulk Flow Variables in 2-Dimensional Rectangular Duct Flow. *Journal of Fluids Engineering-Transactions of the Asme* 100: 215-23

Denis L, Fournier C, Fournel T, Ducottet C. *2005,* 5914: 59140J-40J-14.

Fukagata K, Kasagi N, Koumoutsakos P. 2006. A theoretical prediction of friction drag reduction in turbulent flow by superhydrophobic surfaces. *Physics of Fluids* 18

Garcia-Mayoral R, Jimenez J. 2011. Hydrodynamic stability and breakdown of the viscous regime over riblets. *Journal of Fluid Mechanics* 678: 317-47

Gopalan S, Katz J. 2000. Flow structure and modeling issues in the closure region of attached cavitation. *Physics of Fluids* 12: 895-911

Greidanus AJ, Delfos R, Westerweel J. 2011. Drag reduction by surface treatment in turbulent Taylor-Couette flow. *13th European Turbulence Conference (Etc13): Convection, Rotation, Stratification and Buoyancy Effects* 318

Hasegawa Y, Frohnapfel B, Kasagi N. 2011. Effects of spatially varying slip length on friction drag reduction in wall turbulence. *13th European Turbulence Conference (Etc13): Wall-Bounded Flows and Control of Turbulence* 318

Hong JR, Katz J, Schultz MP. 2011. Near-wall turbulence statistics and flow structures over three-dimensional roughness in a turbulent channel flow. *Journal of Fluid Mechanics* 667: 1-37

Jeffs K, Maynes D, Webb BW. 2010. Prediction of turbulent channel flow with superhydrophobic walls consisting of micro-ribs and cavities oriented parallel to the flow direction. *International Journal of Heat and Mass Transfer* 53: 786-96

Jelly TO, Jung SY, Zaki TA. 2014. Turbulence and skin friction modification in channel flow with streamwise-aligned superhydrophobic surface texture. *Physics of Fluids* 26

Jimenez J. 2004. Turbulent flows over rough walls. *Annual Review of Fluid Mechanics* 36: 173-96

Jung YC, Bhushan B. 2010. Biomimetic structures for fluid drag reduction in laminar and turbulent flows. *Journal of Physics-Condensed Matter* 22

Katz J, Sheng J. 2010. Applications of Holography in Fluid Mechanics and Particle Dynamics. *Annual Review of Fluid Mechanics* 42: 531-55

Lee SH, Sung HJ. 2007. Direct numerical simulation of the turbulent boundary layer over a rod-roughened wall. *Journal of Fluid Mechanics* 584: 125-46

Ligrani PM, Moffat RJ. 1986. Structure of Transitionally Rough and Fully Rough Turbulent Boundary-Layers. *Journal of Fluid Mechanics* 162: 69-98

Ling HJ, Katz J. 2014. Separating twin images and locating the center of a microparticle in dense suspensions using correlations among reconstructed fields of two parallel holograms. *Applied Optics* 53: G1-G11

Liu KS, Tian Y, Jiang L. 2013. Bio-inspired superoleophobic and smart materials: Design, fabrication, and application. *Progress in Materials Science* 58: 503-64

Liu XF, Katz J. 2006. Instantaneous pressure and material acceleration measurements using a four-exposure PIV system. *Experiments in Fluids* 41: 227-40

Liu XF, Katz J. 2013. Vortex-corner interactions in a cavity shear layer elucidated by time-resolved measurements of the pressure field. *Journal of Fluid Mechanics* 728: 417-57

Martell MB, Perot JB, Rothstein JP. 2009. Direct numerical simulations of turbulent flows over superhydrophobic surfaces. *Journal of Fluid Mechanics* 620: 31-41

Martell MB, Rothstein JP, Perot JB. 2010. An analysis of superhydrophobic turbulent drag reduction mechanisms using direct numerical simulation. *Physics of Fluids* 22

Min TG, Kim J. 2004. Effects of hydrophobic surface on skin-friction drag. *Physics of Fluids* 16: L55-L58

Park H, Park H, Kim J. 2013a. A numerical study of the effects of superhydrophobic surface on skin-friction drag in turbulent channel flow. *Physics of Fluids* 25

Park H, Sun GY, Kim CJ. 2013b. Turbulent Drag Reduction on Superhydrophobic Surfaces Confirmed by Built-in Shear Sensing. *26th Ieee International Conference on Micro Electro Mechanical Systems (Mems 2013)*: 1183-86

Park H, Sun GY, Kim CJ. 2014. Superhydrophobic turbulent drag reduction as a function of surface grating parameters. *Journal of Fluid Mechanics* 747: 722-34

Peguero C, Breuer K. 2009. On Drag Reduction in Turbulent Channel Flow over Superhydrophobic Surfaces. *Advances in Turbulence Xii - Proceedings of the 12th Euromech European Turbulence Conference* 132: 233-36

Roth GI, Katz J. 2001. Five techniques for increasing the speed and accuracy of PIV interrogation. *Measurement Science & Technology* 12: 238-45

Rothstein JP. 2010. Slip on Superhydrophobic Surfaces. *Annual Review of Fluid Mechanics* 42: 89-109

Saito N, Pullin DI. 2014. Large eddy simulation of smooth-rough-smooth transitions in turbulent channel flows. *International Journal of Heat and Mass Transfer* 78: 707-20

Samaha MA, Tafreshi HV, Gad-el-Hak M. 2011. Modeling drag reduction and meniscus stability of superhydrophobic surfaces comprised of random roughness. *Physics of Fluids* 23

Samaha MA, Tafreshi HV, Gad-el-Hak M. 2012. Influence of Flow on Longevity of Superhydrophobic Coatings. *Langmuir* 28: 9759-66

Schultz MP, Flack KA. 2007. The rough-wall turbulent boundary layer from the hydraulically smooth to the fully rough regime. *Journal of Fluid Mechanics* 580: 381-405

Seo J, Garcia-Mayoral R, Mani A. 2015. Pressure fluctuations and interfacial robustness in turbulent flows over superhydrophobic surfaces. *Journal of Fluid Mechanics* 783: 448-73

Seo J, Mani A. 2015. On the scaling of the slip velocity in turbulent fows over superhydrophobic surfaces. *Physics of Fluids* submitted

Sheng J, Malkiel E, Katz J. 2008. Using digital holographic microscopy for simultaneous measurements of 3D near wall velocity and wall shear stress in a turbulent boundary layer. *Experiments in Fluids* 45: 1023-35

Sheng J, Malkiel E, Katz J. 2009. Buffer layer structures associated with extreme wall stress events in a smooth wall turbulent boundary layer. *Journal of Fluid Mechanics* 633: 17-60

Shirtcliffe NJ, McHale G, Newton MI. 2011. The Superhydrophobicity of Polymer Surfaces: Recent Developments. *Journal of Polymer Science Part B-Polymer Physics* 49: 1203-17

Shockling MA, Allen JJ, Smits AJ. 2006. Roughness effects in turbulent pipe flow. *Journal of Fluid Mechanics* 564: 267-85

Smits AJ. 2010. High Reynolds Number Wall-Bounded Turbulence and a Proposal for a New Eddy-Based Model. *Turbulence and Interactions* 110: 51-62

Srinivasan S, Chhatre SS, Mabry JM, Cohen RE, McKinley GH. 2011. Solution spraying of poly(methyl methacrylate) blends to fabricate microtextured, superoleophobic surfaces. *Polymer* 52: 3209-18

Srinivasan S, Kleingartner JA, Gilbert JB, Cohen RE, Milne AJB, McKinley GH. 2015. Sustainable Drag Reduction in Turbulent Taylor-Couette Flows by Depositing Sprayable Superhydrophobic Surfaces. *Physical Review Letters* 114

Talapatra S, Katz J. 2013. Three-dimensional velocity measurements in a roughness sublayer using microscopic digital in-line holography and optical index matching. *Measurement Science & Technology* 24

Tian H, Zhang J, Wang E, Yao Z, Jiang N. 2015. Experimental investigation on drag reduction in turbulent boundary layer over superhydrophobic surface by TRPIV. *Theoretical and Applied Mechanics Letters* 5: 45-49

Unal UO, Unal B, Atlar M. 2012. Turbulent boundary layer measurements over flat surfaces coated by nanostructured marine antifoulings. *Experiments in Fluids* 52: 1431-48

Watanabe K, Yanuar, Udagawa H. 1999. Drag reduction of Newtonian fluid in a circular pipe with a highly water-repellent wall. *Journal of Fluid Mechanics* 381: 225-38

Woolford B, Prince J, Maynes D, Webb BW. 2009. Particle image velocimetry characterization of turbulent channel flow with rib patterned superhydrophobic walls. *Physics of Fluids* 21

Yang J, Zhang ZZ, Xu XH, Men XH, Zhu XT, Zhou XY. 2011. Superoleophobic textured aluminum surfaces. *New Journal of Chemistry* 35: 2422-26

You D, Moin P. 2007. Effects of hydrophobic surfaces on the drag and lift of a circular cylinder. *Physics of Fluids* 19

Zhao J-p, Du X-d, Shi X-h. 2007. Experimental research on friction-reduction with super-hydrophobic surfaces. *Journal of Marine Science and Application* 6: 58-61

#	1 △	2 ▲	3 ▼	4 ×	5 ▷	6 ◁	7 □	8 ■	9 ◆	10 ☆	11 ✡	12 ✶	13 ▨
Sample	Smooth	SHS_{Por}	SHS_{Por}	SHS_{Alr}	SHS_{Alx}	SHS_{Alx}	Smooth	SHS_{Por}	SHS_{Por}	Smooth	Smooth	SHS_{Por}	SHS_{Alx}
CA, ±2°	-	156 (148)	148 (120)	153 (150)	153 (143)	147 (147)	-	159	159	-	-	159	148 (140)
SA, ±1°	-	2	5	8	8	8	-	2	2	-	-	2	8
k_{rms}, µm	-	4.8	4.8	10.9	8.9	8.9	-	7.8	20.4	-	-	13.7	8.9
ΔP, kPa	-	− 0.3	20.0	4.0	4.0	20.0	-	− 0.3	− 0.3	-	-	− 0.3	− 0.3
x, mm	70	70	70	70	70	70	70	70	70	70	70	70	35
U_m, m/s	2.0							2.0		5.5	5.9		2.0
U_0, m/s	2.2							2.2		6.0	6.4		2.2
δ_{99}, mm	9.1							16.6		7.4	18.8		9.1
Re_δ	20 020							36 520		44 400	120 320		20 020
τ_w^{μ}, Pa	9.0	7.9 ±0.0	7.8 ±0.0	5.3 ±0.0	4.9 ±0.0	4.1 ±0.0	7.2	6.0 ±0.0	4.0 ±0.1	51	52	14.6 ±1.3	4.0 ±0.0
τ_w^{R}, Pa	0	0.0 ±0.0	0.4 ±0.1	1.2 ±0.4	0.9 ±0.5	3.0 ±0.4	0	0.4 ±0.1	3.0 ±0.5	0	0	42.6 ±4.1	1.7 ±0.8
τ_w, Pa	9.0	7.9 ±0.1	8.2 ±0.1	6.6 ±0.4	5.8 ±0.5	7.1 ±0.4	7.2	6.4 ±0.1	7.0 ±0.3	51	52	57.2 ±2.8	5.8 ±0.8
τ_w^{Log}, Pa	9.0	9.2	9.4	8.5	8.1	8.6	7.3	7.4	7.7	51	51	64	9.0
τ_t^{max}, Pa	9.0	8.6	8.7	8.6	8.2	8.7	7.3	6.9	7.5	52	52	63	8.6
u_τ, m/s	0.095	0.089	0.091	0.081	0.076	0.084	0.085	0.080	0.084	0.226	0.228	0.239	0.076
δ_υ, µm	10.5	11.3	11.0	12.3	13.1	11.9	11.8	12.5	12.0	4.43	4.39	4.18	13.1
$\bar{U}_s$, m/s	-	0.30 ±0.02	0.29 ±0.03	0.58 ±0.03	0.71 ±0.02	0.75 ±0.03	-	0.35 ±0.02	0.67 ±0.04	-	-	2.08 ±0.08	0.73 ±0.02
Re_τ	863	809	824	739	693	767	1408	1328	1389	1671	4287	4496	693
k_{rms}^{+}	-	0.43	0.43	0.89	0.68	0.75	-	0.62	1.71	-	-	3.28	0.67
ΔU^{+}	-	1.1	0.8	3.0	4.5	2.6	-	1.1	0	-	-	−2.2	4.5
$\bar{U}_s^{+}$	-	3.4 ±0.2	3.2 ±0.3	7.1 ±0.4	9.3 ±0.3	8.9 ±0.4	-	4.4 ±0.3	8.0 ±0.5	-	-	8.7 ±0.3	9.6 ±0.3
DR	-	0.12	0.09	0.27	0.36	0.21	-	0.11	0.03	-	-	−0.10	0.36

TABLE 1. A summary of experimental conditions and measured parameters for all tests included in this paper. *CA* denotes the contact angle, *SA* the sliding angle, and *DR* the drag reduction. Values of *CA* in parenthesis are contact angles measured after the experiment and exposing the wall to air. The same symbols apply for all the figures.

Movie 1: Sample original holograms recorded at 20 kHz in the JHU water tunnel showing a sample plastron for a turbulent boundary over SHS_{Por}, a porous substrate spray-coated with F-POSS/PMMA. The rms value of roughness height is 10 µm, the freestream velocity is 2.2 m/s, the friction Reynolds number is 1408, and the pressure difference across the porous base is 12 kPa (higher above the SHS). Image size: 9.3 mm×2.5 mm.

Movie 2: Sample original holograms recorded at 20 kHz in the JHU water tunnel showing a sample plastron for a turbulent boundary over SHS_{Por}, a porous substrate spray-coated with F-POSS/PMMA. The rms value of roughness height is 10 µm, the freestream velocity is 4.3 m/s, the friction Reynolds number is about 2850, and the pressure difference across the porous base is 6 kPa (higher above the SHS). Image size: 9.3 mm×2.5 mm.

Movie 3: Sample original holograms recorded at 20 kHz in the JHU water tunnel showing a sample plastron for a turbulent boundary over SHS_{Por}, a porous substrate spray-coated with F-POSS/PMMA. The rms value of roughness height is 10 µm, the freestream velocity is 6.4 m/s, the friction Reynolds number is 4287, and the pressure difference across the porous base is −4 kPa (higher below the SHS). Image size: 9.3 mm×2.5 mm.

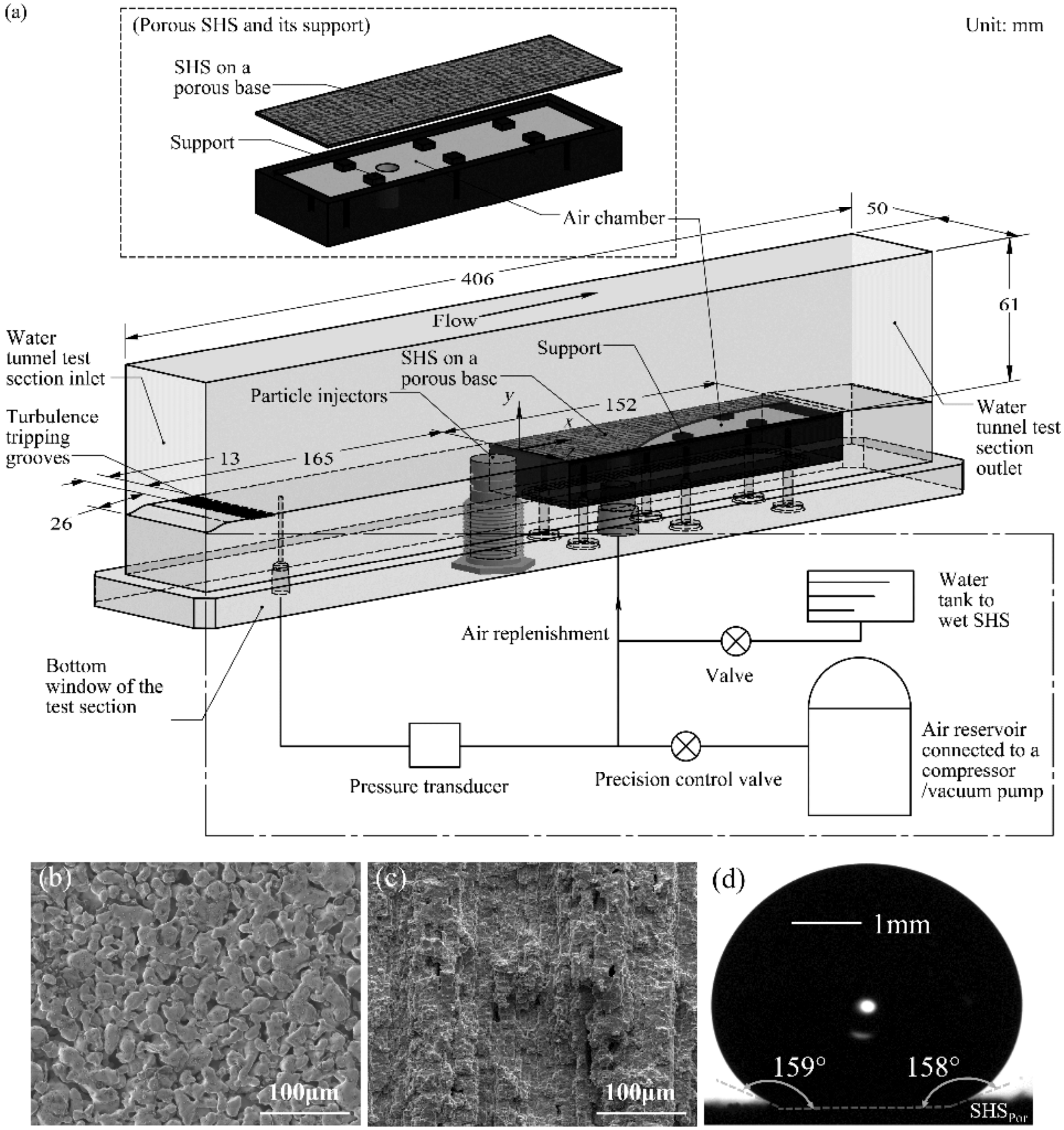

Figure 1. (a) The test section and the pressure control/measurement system; all dimensions are in *mm*; (b) a sample SEM image of SHS_{Por} prior to spray-coating it with F-POSS/PMMA; (c) a sample SEM image of SHS_{Alx} with the streamwise etched grooves; and (d) a sample image of a ~270µL water droplet on SHS_{Por} showing the equilibrium contact angles.

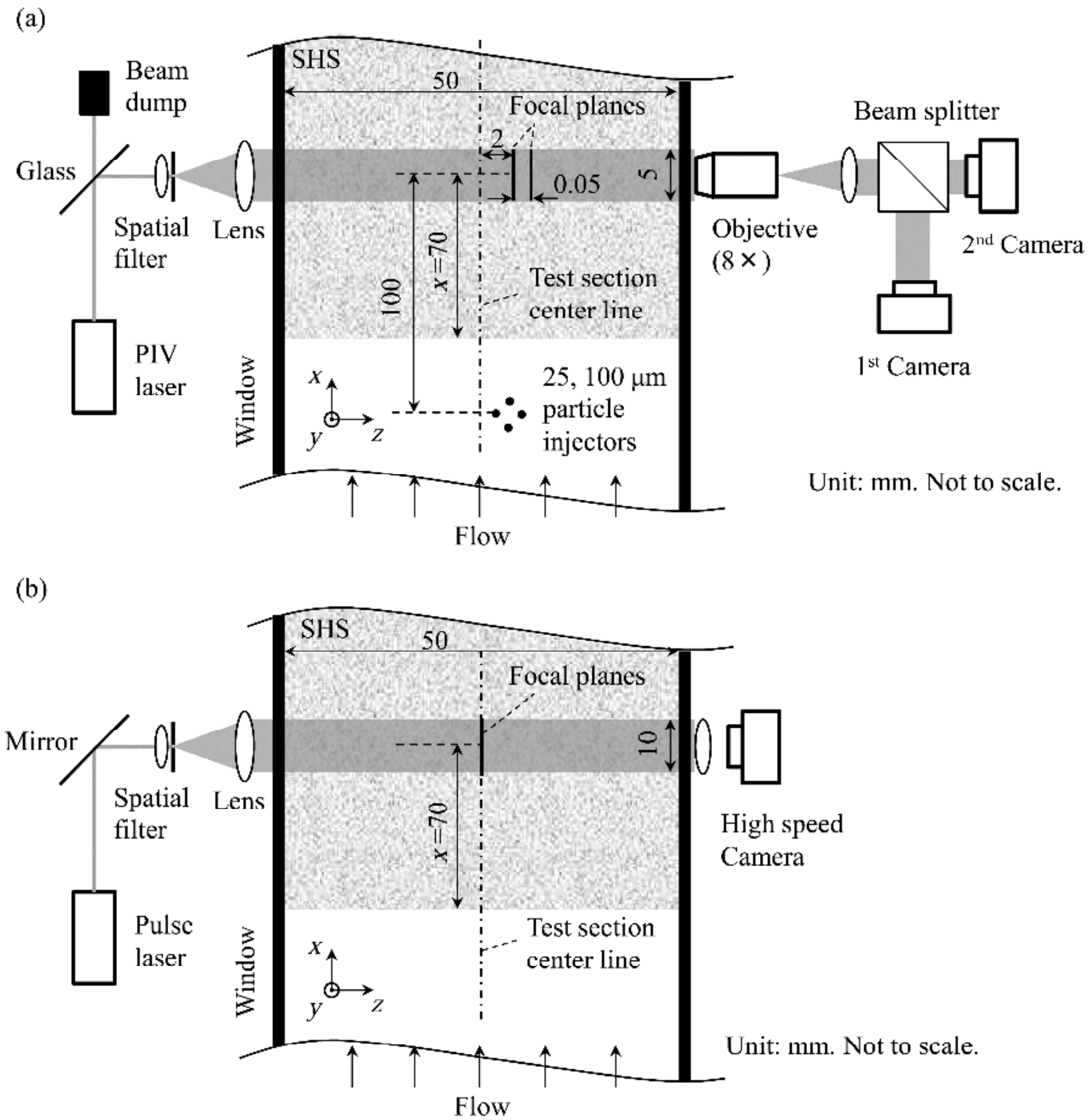

Figure 2. Illustrations of (a) the dual view in-line digital holographic microscopy setup for high-resolution velocity measurements; and (b) the holographic setup for imaging the air layer or ‘plastron’ present on the SHSs.

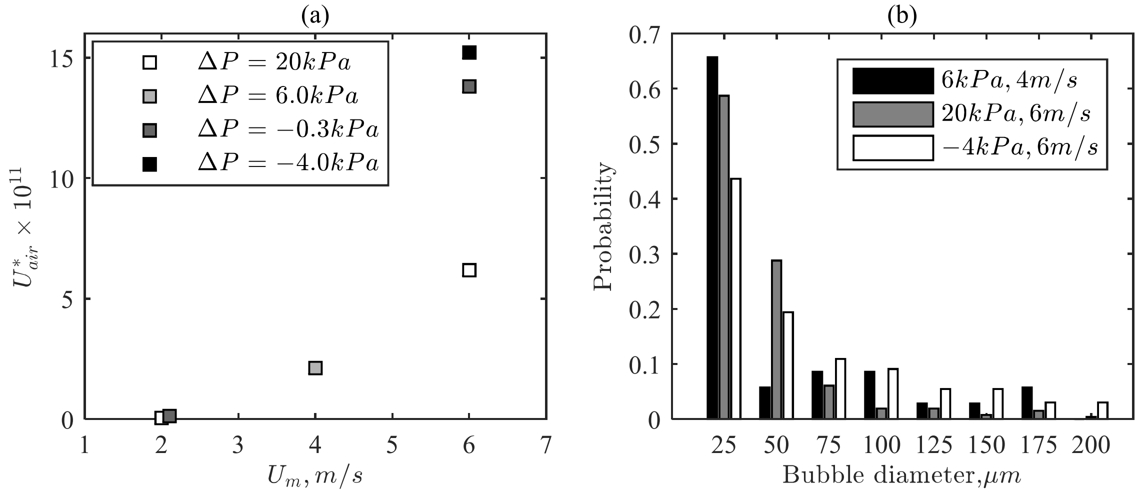

Figure 3. (a) Normalized entrainment rate of air (U^*_{air}) from the SHS$_{\text{Por}}$ upstream of the sample area for several pressure differences across the porous wall; (b) the measured size distribution of the entrained bubbles.

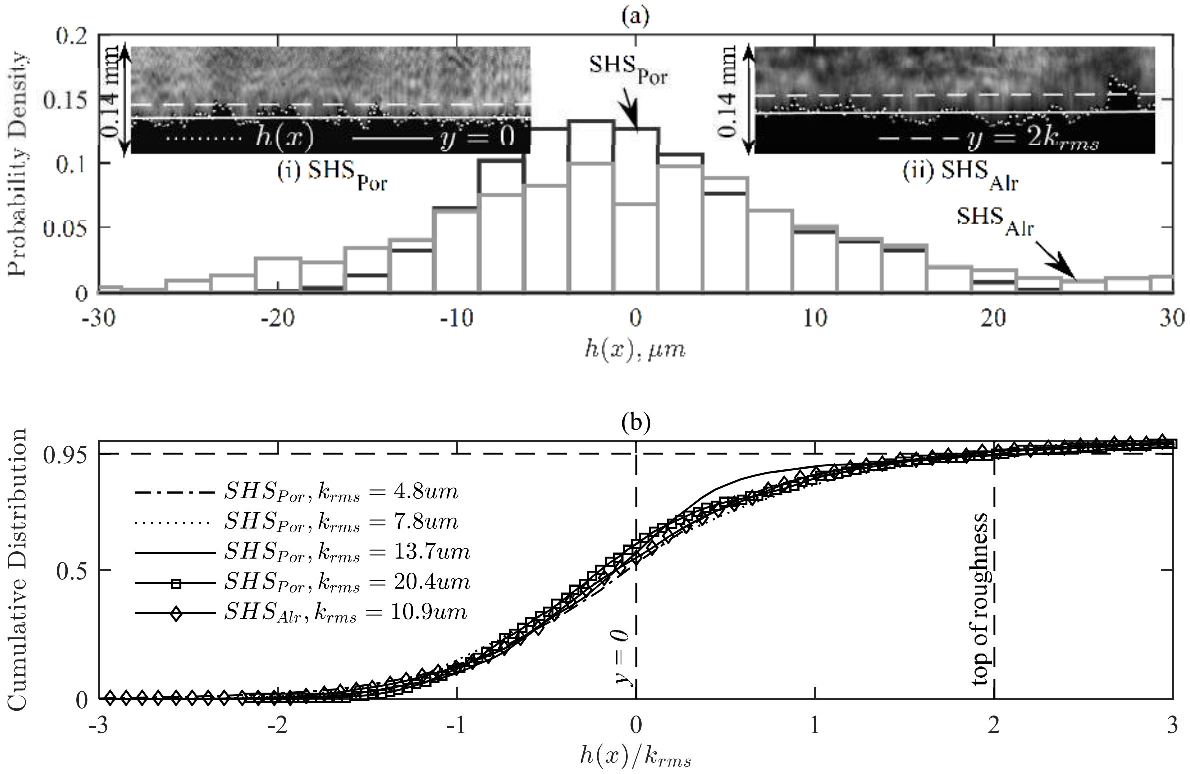

Figure 4. (a) Sample probability density functions of the roughness height *h(x)* for one of the SHS$_{\text{Por}}$ (k_{rms}=7.8 µm, case #8) and the SHS$_{\text{AIr}}$ (case #4). The insets show corresponding sample holograms. Dotted lines: *h(x)*, solid lines: mean roughness height (y = 0), and dashed lines: y=2k_{rms}. (b) Cumulative distribution of *h(x)* for several k_{rms}.

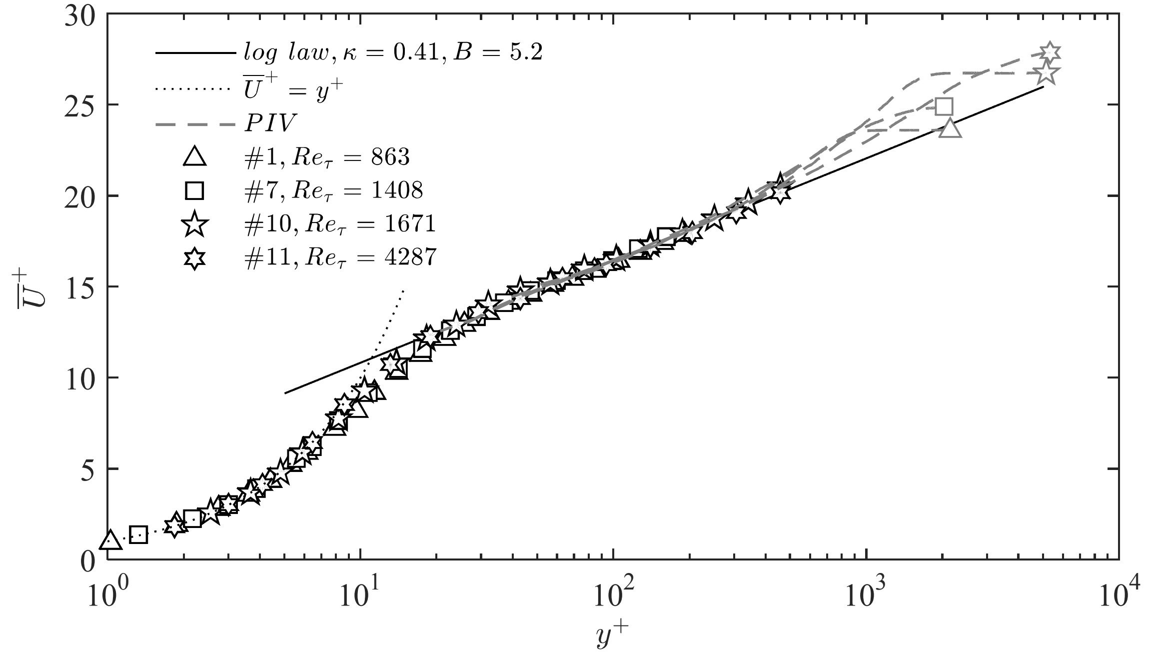

Figure 5. Mean velocity profiles for the baseline (smooth wall) cases. Symbols are consistent with those in table 1. Gray dashed lines and symbols are obtained from 2D PIV, and black symbols show DHM data.

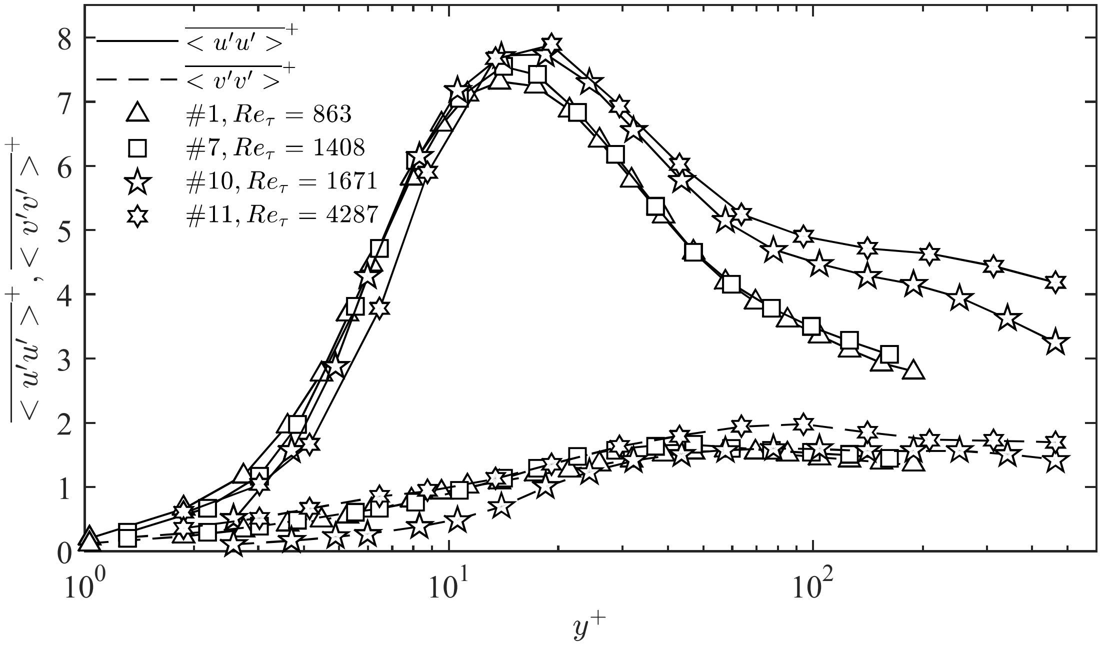

Figure 6. Baseline statistics of streamwise and wall-normal velocity fluctuations.

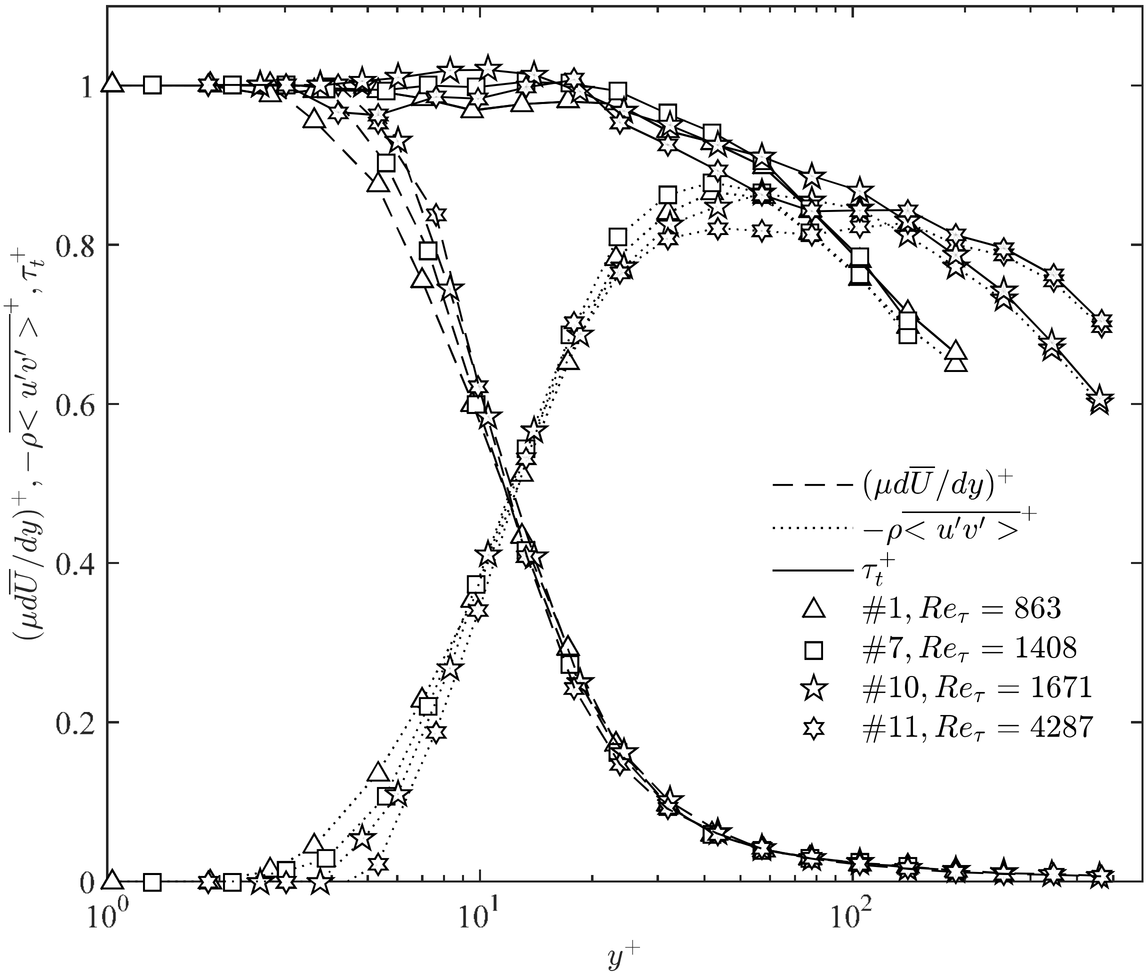

Figure 7. Profiles of baseline viscous shear stress (dashed lines), Reynolds shear stresses (dotted lines), and total shear stress (solid lines).

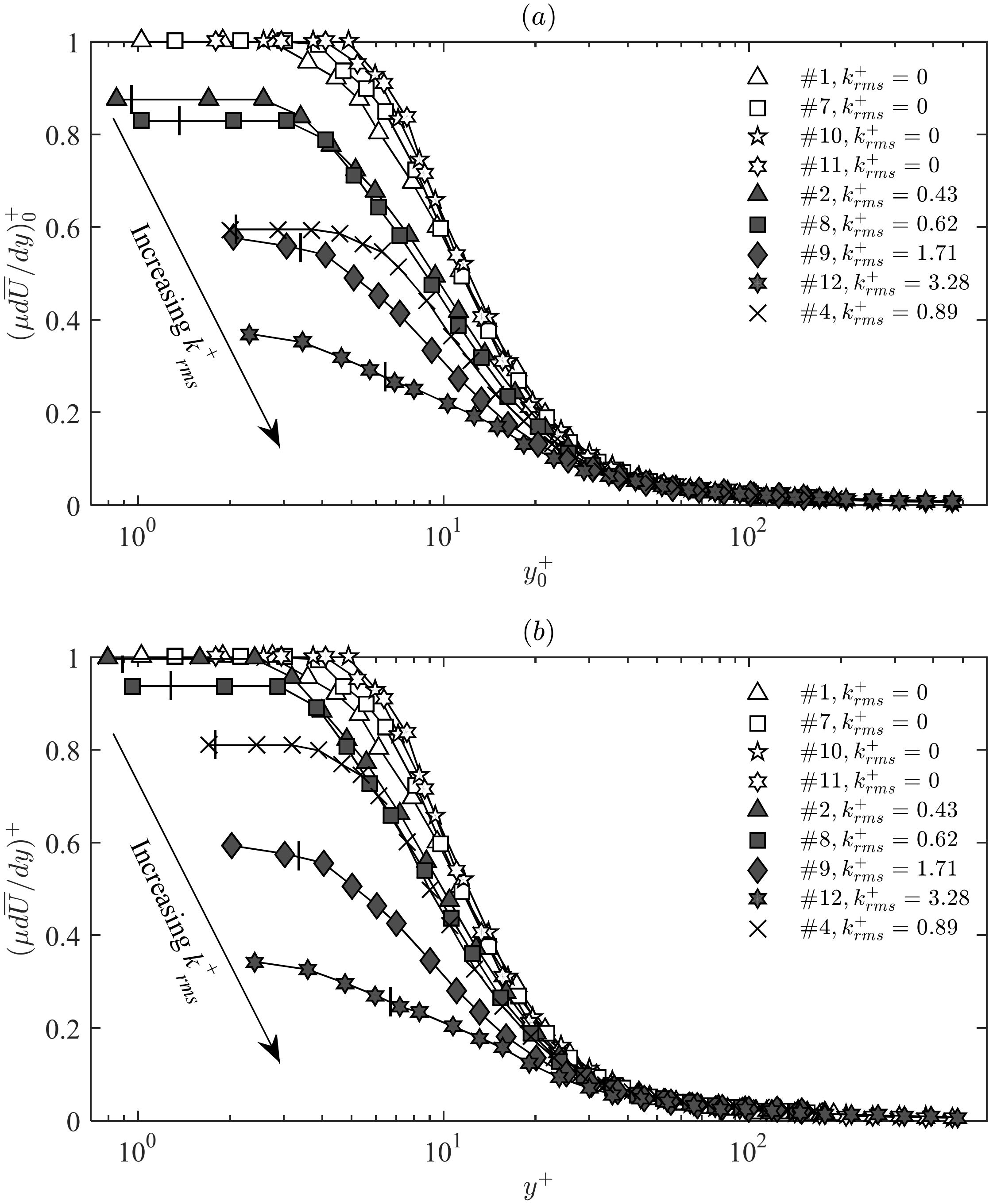

Figure 8. Profiles of viscous shear stress for the SHS$_{\mathrm{Por}}$ (gray symbols) and SHS$_{\mathrm{Alr}}$ (cross) and corresponding baseline cases (hollow symbols) for different values of $k_{rms}{}^+$. Results are scaled by: (a) the smooth wall inner units, and (b) their own inner units. The location of y=2k_{rms} for each profile is marked by a short vertical line.

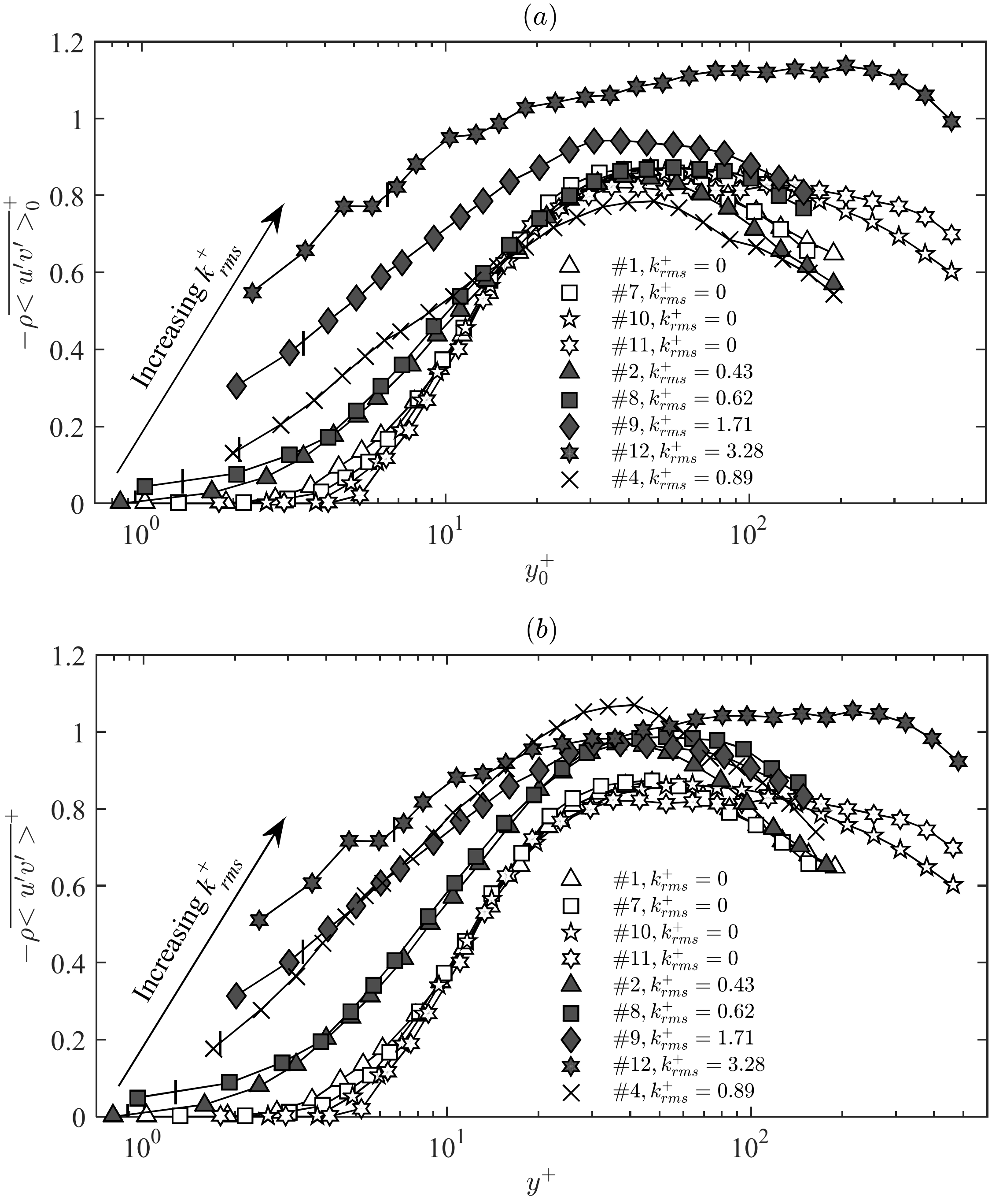

Figure 9. Profiles of Reynolds shear stresses for the $\mathrm{SHS_{Por}}$ (gray symbols) and $\mathrm{SHS_{Alr}}$ (cross) and corresponding baseline cases (hollow symbols) scaled by: (a) the smooth wall inner units, and (b) their own inner units.

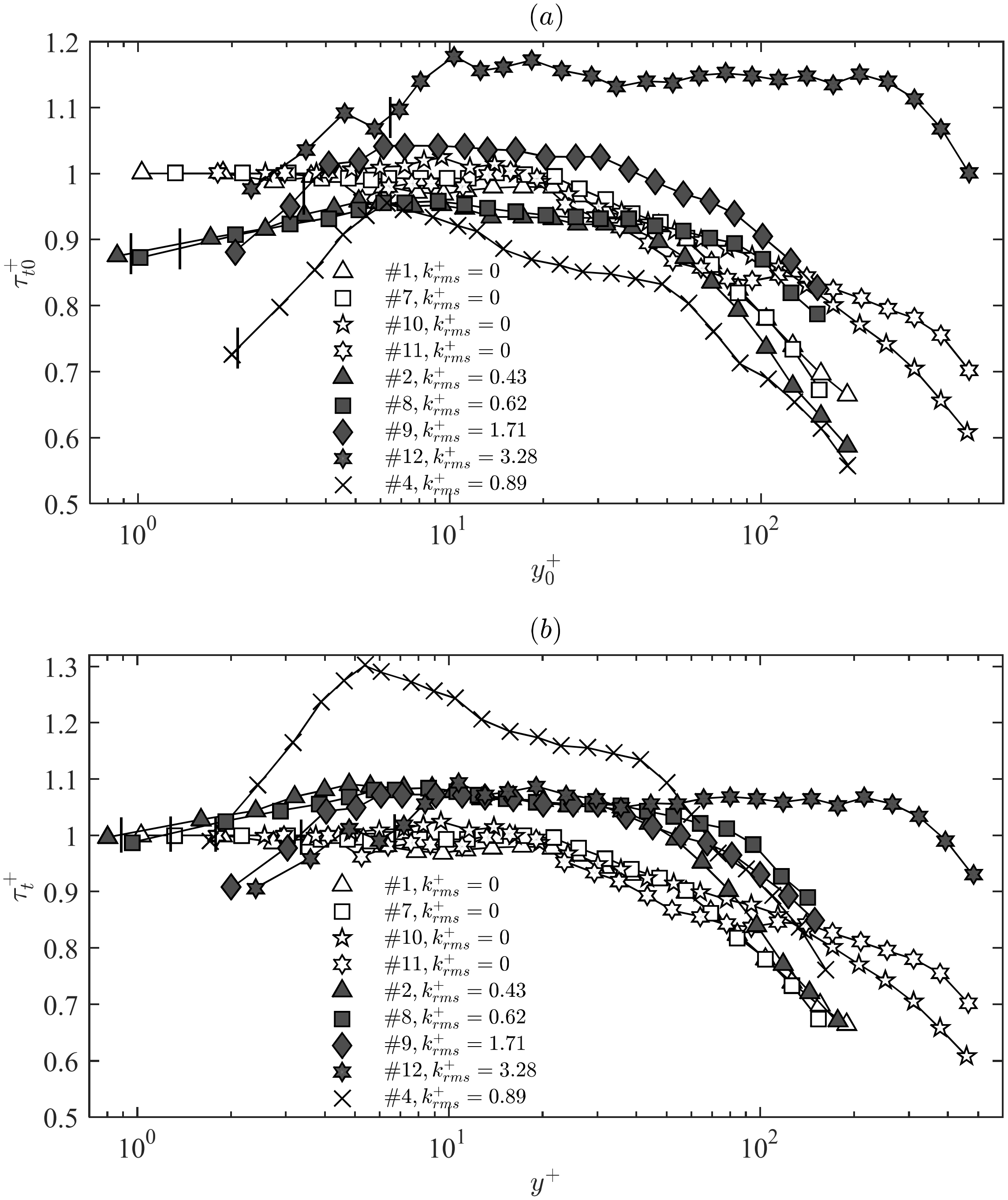

Figure 10. Profiles of total shear stresses scaled by: (a) the smooth wall inner units, and (b) their own inner units. For symbols, refer to table 1 and figures 8.

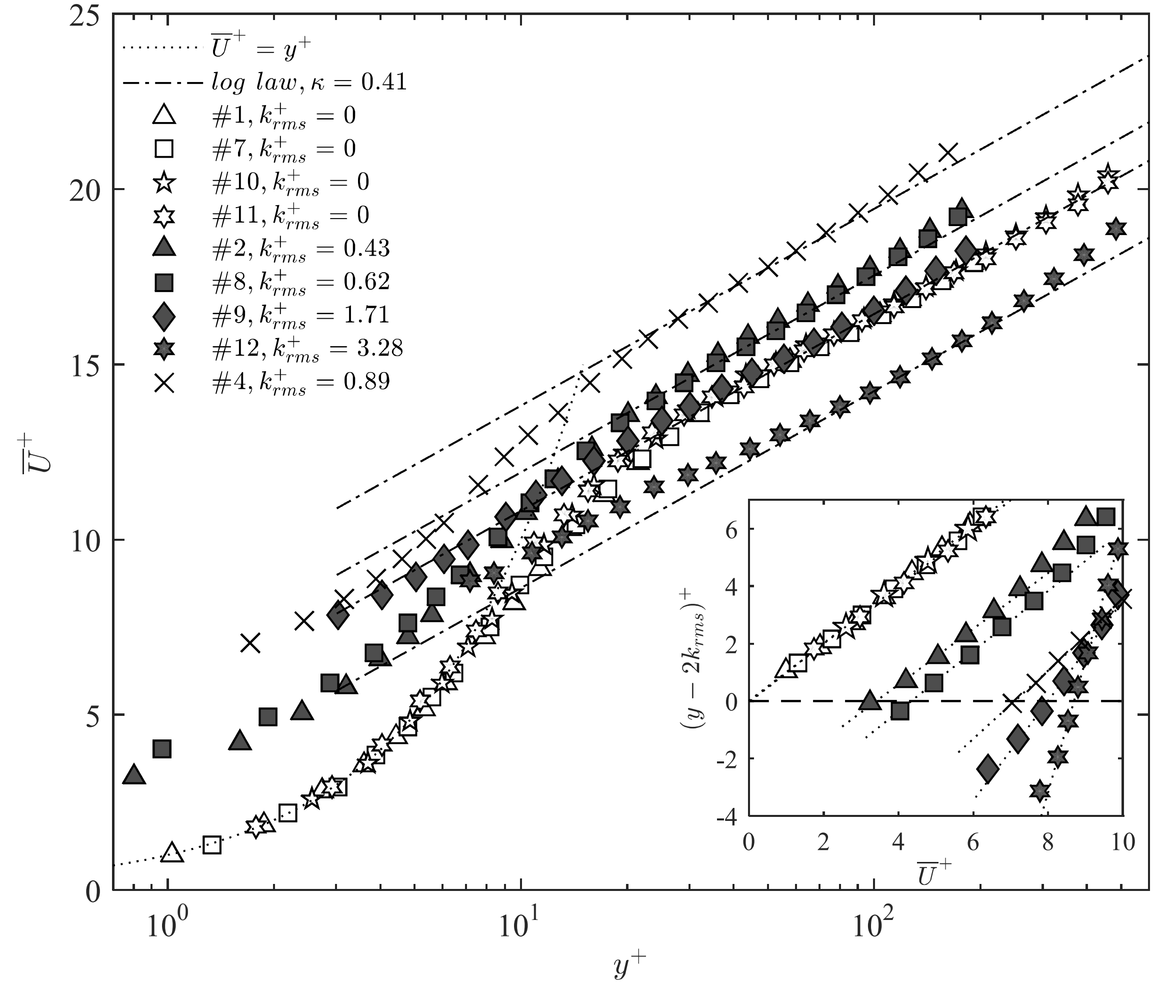

Figure 11. Mean velocity profiles for the SHS$_{Por}$ (gray symbols), SHS$_{Air}$ (cross), and baseline (white symbols) cases scaled by their own inner units. The insert shows the near wall profiles in linear scales, with dotted lines indicating linear least-square fits. Symbol legends are provided in table 1.

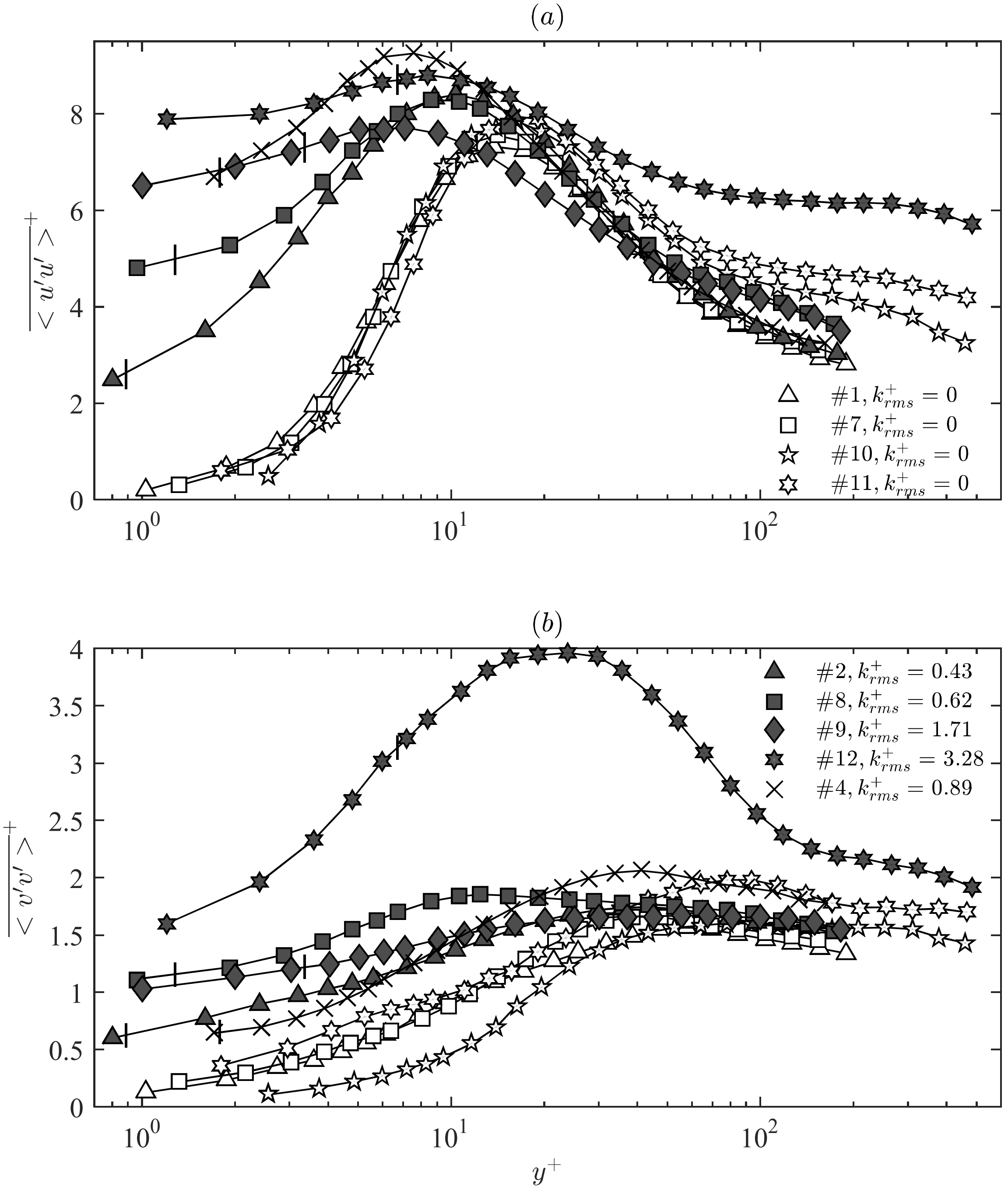

Figure 12. (a) Streamwise, and (b) wall-normal velocity fluctuations normalized by their own inner units.

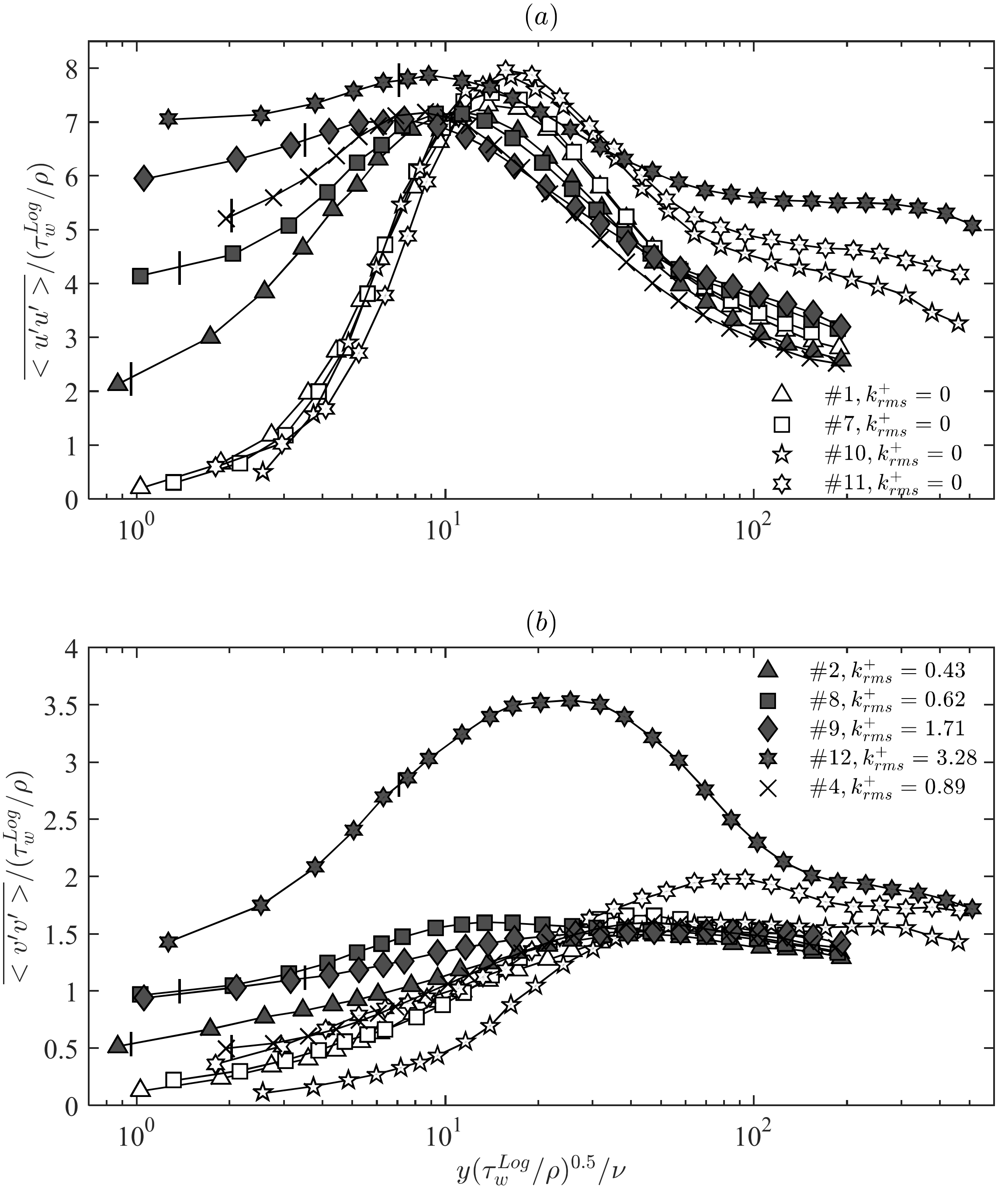

Figure 13. (a) Streamwise, and (b) wall-normal velocity fluctuations normalized by shear stress estimated from a fit to the mean velocity in the log region.

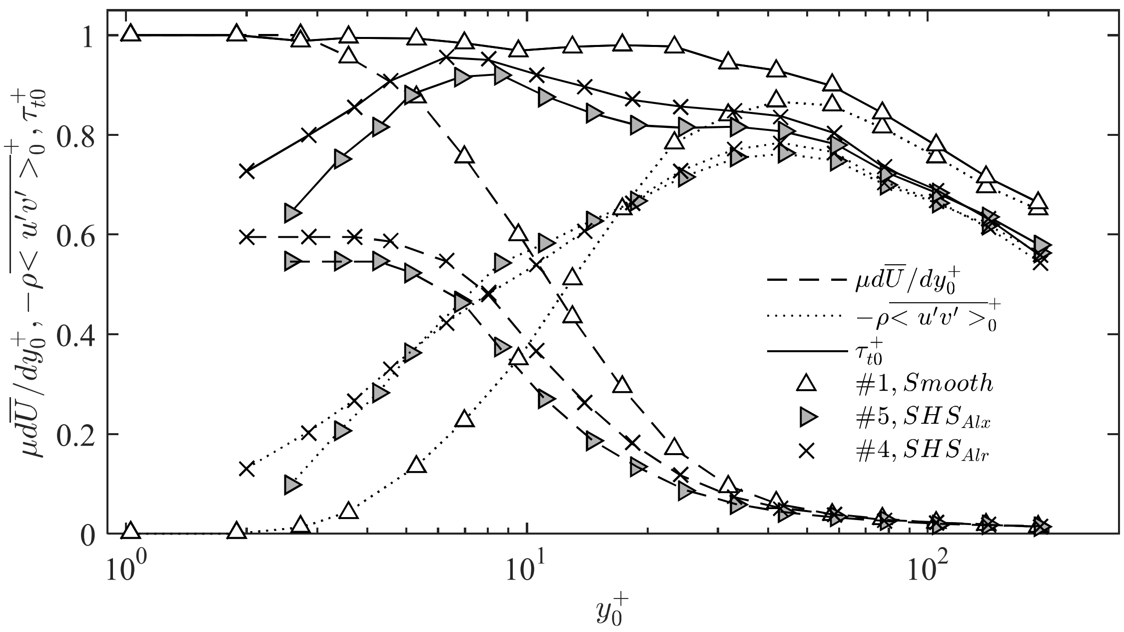

Figure 14. Effects of groove alignment on the etched aluminum surfaces on the viscous, Reynolds and total shear stresses scaled by smooth wall inner units.

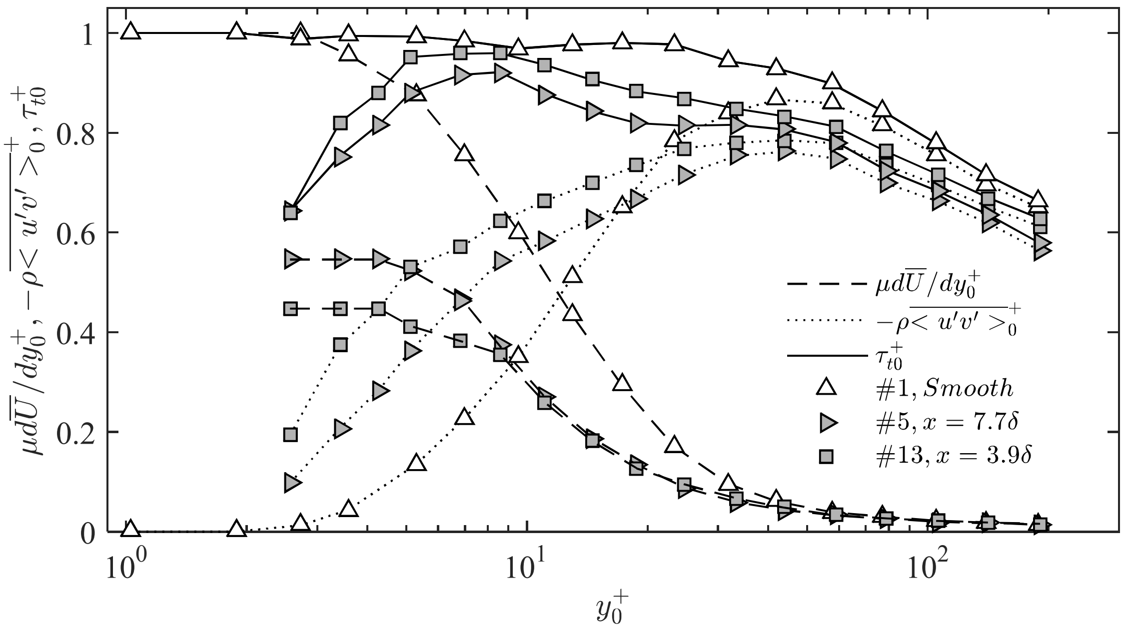

Figure 15. Effects of streamwise distance on the viscous, Reynolds and total shear stresses.

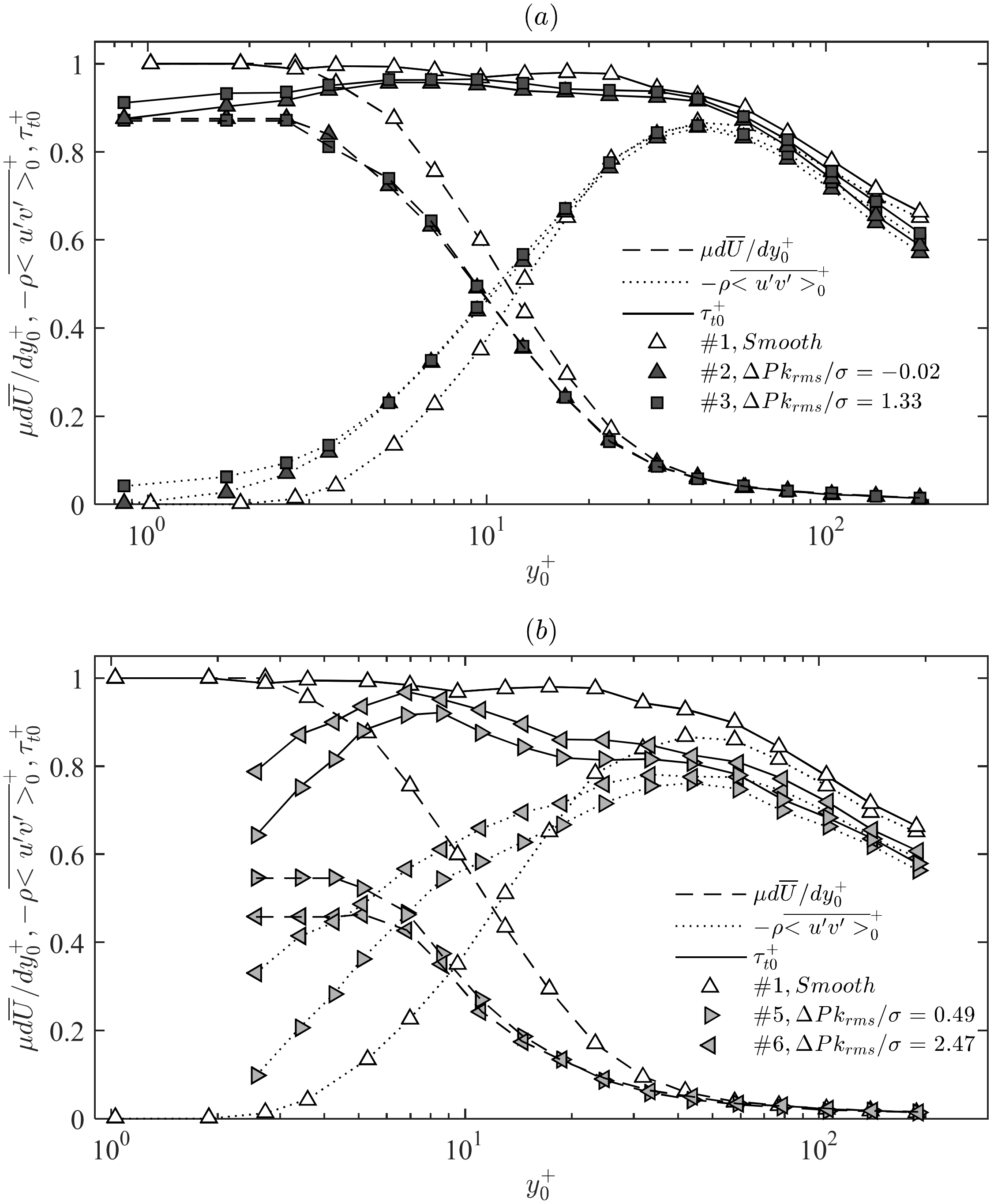
(a)
$\mu d\overline{U}/dy_0^+, -\rho\overline{<u'v'>_0}^+, \tau_{t0}^+$
y_0^+
10^0
10^1
10^2
0
0.2
0.4
0.6
0.8
1
$\mu d\overline{U}/dy_0^+$
$-\rho\overline{<u'v'>_0}^+$
τ_{t0}^+
$\#1, Smooth$
$\#2, \Delta Pk_{rms}/\sigma = -0.02$
$\#3, \Delta Pk_{rms}/\sigma = 1.33$
(b)
$\mu d\overline{U}/dy_0^+, -\rho\overline{<u'v'>_0}^+, \tau_{t0}^+$
y_0^+
10^0
10^1
10^2
0
0.2
0.4
0.6
0.8
1
$\mu d\overline{U}/dy_0^+$
$-\rho\overline{<u'v'>_0}^+$
τ_{t0}^+
$\#1, Smooth$
$\#5, \Delta Pk_{rms}/\sigma = 0.49$
$\#6, \Delta Pk_{rms}/\sigma = 2.47$

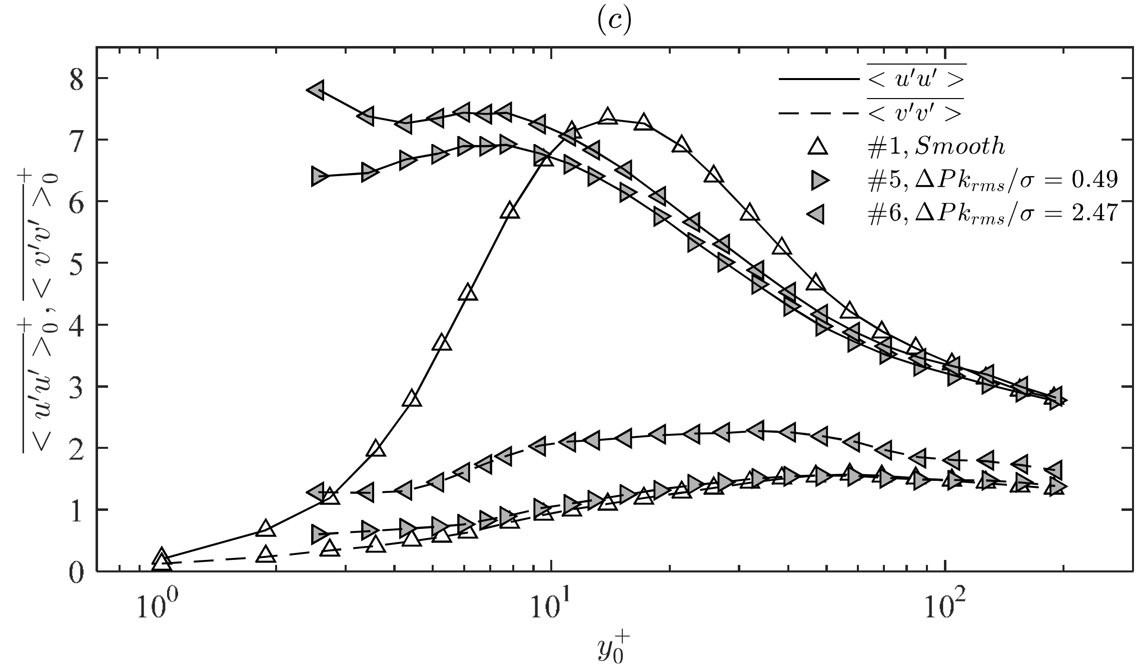

Figure 16. (a) Effects of pressure difference across the porous wall on the shear stresses above the $\mathrm{SHS_{Por}}$; and effects of pressure on (b) the shear stress and (c) streamwise and wall-normal velocity fluctuations above the $\mathrm{SHS_{Alx}}$.

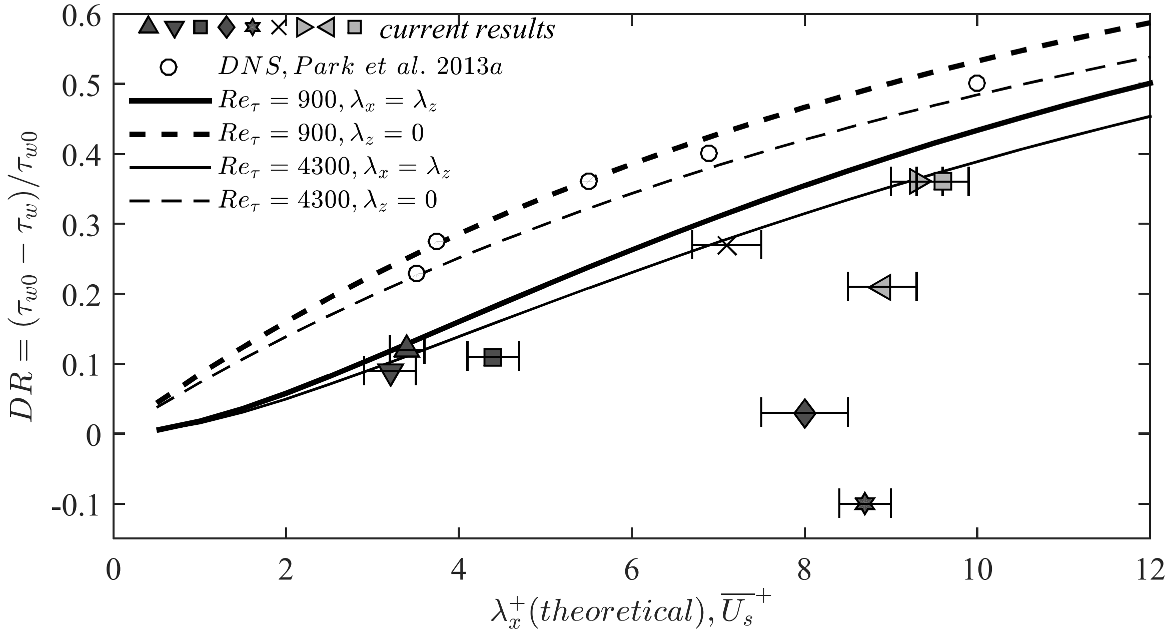

Figure 17. Symbols (table 1) show the measured drag reduction as a function of dimensionless slip velocity in comparison to theoretical prediction (lines) based on equation (2), using the empirical values of $F(\lambda_z^+)$ of Busse & Sandham (2012). Circles show DNS results by Park *et al.* (2013a) for broadly spaced streamwise grooves.